" Manuscript Number: 8217R1 - CORRECTION: February 22, 2022"

Hydrothermal Alteration of Ni-rich Sulfides in Peridotites of Abu Dahr, Eastern Desert, Egypt: Relationships amongst minerals in the Fe-Ni-Co-O-S system, fO_2 and fS_2

Ali H. Abdel-Halim

Department of Geology, Faculty of Science, Minia University, Minia 61519, Egypt

*Corresponding author E-mail: alihelmy@yahoo.com

Abstract

The Neoproterozoic peridotites of Abu Dahr, Eastern Desert of Egypt, consist mainly of highly depleted harzburgites that have experienced multiple stages of serpentinization (lizarditization and antigoritization) and carbonation/listvenitization in a forearc environment. The Abu Dahr forearc harzburgites are more oxidized than oceanic mantle, with the oxygen fugacity (fO_2) values ranging from FMQ +0.41 to FMQ +1.20 (average = +0.60 FMQ), and were equilibrated at temperatures of 910-1217°C and pressures of 4.1-7.8 kbar. This study has documented for the first time the presence of a variety of Ni-rich Ni-Fe (-Co) sulfide and metal phases along with Fe-oxides/oxyhydroxides in serpentinized-carbonated peridotites of the Abu Dahr forearc. Here I concentrate on the relationship between redox state and Fe-Ni-Co-O-S minerals with emphasis on the role of hydrothermal processes in upgrading magmatic sulfide tenors, desulfurization (sulfur-loss) of magmatic pentlandite and hydrothermal upgrading of the sulfide phases in Abu Dahr forearc environment. The minerals involved are high-Ni pentlandite ($Fe_4Ni_5S_8$), cobaltian pentlandite ($Fe_{3.47}Ni_{4.78}Co_{0.75}S_8$), heazlewoodite ($Fe_{0.07}Ni_{2.93}S_2$), godlevskite ($Fe_{0.26}Ni_{8.73}Co_{0.01}S_8$), millerite ($Fe_{0.01}Ni_{0.98}Cu_{0.01}S$), awaruite ($Ni_{75}Fe_{21}$) and native Ni ($Ni_{93}Fe_5$), and nickeliferous magnetite and goethite. Chalcopyrite is a rare mineral; other Cu-phases, Fe-sulfides and Ni-arsenides/phosphides are not present. Texturally, Ni-sulfide and alloy

minerals occur as interstitial disseminated blebs of either solitary phases or composite intergrowths with characteristic replacement textures, documenting strong variations in oxygen and sulfur fugacities (fO_2-fS_2). Sulfide assemblages are divided into three main facies: (1) pentlandite-rich; (2) godlevskite-rich; and (3) millerite-rich. Textural relationships imply the following sequence: (a) primary pentlandite → cobaltian pentlandite, with partial replacement of the latter by awaruite and/or heazlewoodite along with magnetite; (b) heazlewoodite is replaced by godlevskite, which in turns is replaced by millerite; (c) Ni-rich awaruite breaks down to millerite; and finally, (d) magnetite is completely replaced by goethite. The sulfide mineralogy reflects the magmatic and post-magmatic evolution of the complex. The primary magmatic processes gave rise to pentlandite, whereas the secondary Ni-sulfides together with the metallic alloys formed in response to changing fO_2 and fS_2 conditions associated with post-magmatic serpentinization and carbonation. Serpentinization-related Ni-Fe-Co remobilization from magmatic olivines resulted in; (1) upgrading the Ni-Co tenors of pre-existing primary pentlandite, and desulfidation to form low-sulfur sulfides (mainly heazlewoodite) and awaruite under extremely low fO_2 and fS_2 conditions; 2) *in-situ* precipitation of secondary Ni-sulfides in the presence of extra sulfur as aqueous H_2S derived from the desulfurization of magmatic pentlandite or, native Ni when fS_2 approaches 0; 3) transformation from low-sulfur pentlandite- and godlevskite-rich assemblages to the high-sulfur millerite-rich assemblages related to later carbonation with increasing fO_2; and 4) partial dehydration of antigorite serpentinites under high-pressure conditions (> 1GPa) generated Ni-rich awaruite in equilibrium with the prograde assemblage antigorite-metamorphic olivine at higher fO_2 and fS_2 within subduction channel. The mineralogical, chemical, and thermal similarities with other serpentinite-related Ni-sulfides

worldwide suggest that Ni minerals in the Fe-Ni-Co-O-S system record changing fO_2 and fS_2 during progressive serpentinization and carbonation.

Keywords: Abu Dahr forearc, Ni-rich sulfides, oxygen and sulfur fugacities, replacement textures, serpentinization and carbonation, desulfurization, subduction channel.

Introduction

Peridotite serpentinization and carbonation play important roles in upgrading the mineralogy and tenor (i.e. the Ni content of the sulfide fraction) of pre-existing primary Ni-sulfides. Serpentinization is accompanied by the formation of magnetite and release of Ni, Fe, and Co from the primary silicates (e.g. olivine) (Groves et al., 1974; Eckstrand, 1975; Donaldson, 1981; Kamenetsky et al., 2016). Ni released from olivine during serpentinization may be added to or substituted for Fe in the pre-existing sulfide phases (e.g. pentlandite), producing high-Ni tenor pentlandite and/or precipitation of new hydrothermal sulfides when enough H_2S is available (e.g. Eckstrand, 1975; Donaldson, 1981; Keays and Jowitt, 2013). Sulfide and metal mineralogy during hydrothermal alteration reflect strong variations in fluid redox conditions, i.e., variations in oxygen fugacity (fO_2) and sulfur fugacity (fS_2) (Frost, 1985; Alt and Shanks 1998; Marques et al., 2007; Klein and Bach, 2009; Schwarzenbach et al., 2012, 2014, 2021; Foustoukos et al., 2015; de Obeso and Kelemen, 2020). Initial serpentinization, with relict primary mantle minerals (olivine, orthopyroxene and clinopyroxene) along with the low-sulfur assemblage pentlandite-heazlewoodite-awaruite represents a highly reducing and extremely low fO_2 and fS_2 environment (Eckstrand, 1975; Alt and Shanks, 1998; Schwarzenbach et al., 2014). Completely serpentinized peridotites preserve high-sulfur assemblages and magnetite (Eckstrand, 1975; Alt and Shanks, 1998; Schwarzenbach et al., 2014). Talc-carbonate alteration also results in the enrichment of Ni in talc and, at high sulfur activity, millerite grows at the expense of the low-sulfur sulfides

(heazlewoodite and godlevskite) (e.g. Donaldson, 1981; Marques et al., 2007; Klein and Bach, 2009; Schwarzenbach et al., 2014). Therefore, hydrothermal Ni-upgrading might cause the ophiolitic serpentinized peridotites to be viewed as prospective for Ni deposits.

Several serpentinite-hosted Ni deposits such as the Dumont Sill, Quebec (Eckstrand, 1975; Sciortino et al., 2015), Bou Azzer, Morocco (Ahmed et al., 2009), Avebury Ni sulfide deposit, Tasmania (Keays and Jowitt, 2013; Kamenetsky et al., 2016), Hayachine, Japan (Shiga, 1987), Eastern Metals, Canada (Auclair et al., 1993), Epoch deposit, Zimbabwe (Pirajno and González-Álvarez, 2013), Doriri Creek deposit, Papua, New Guinea (González-Álvarez et al., 2013), Elizabeth Hill, Western Australia (Hoatson and Sun, 2002), Black Swan, Western Australia (Barnes et al., 2009), and Sarah's Find Ni-Cu-(PGE) deposit, Western Australia (Le Vaillant et al., 2016) have been interpreted as having hydrothermal origins.

The oxidation state of the forearc mantle wedge is attributed either to oxidizing components, derived from subducted slab and added to the mantle wedge cause metasomatic changes and/or partial melting (Evans, 2006, 2012; Bénard et al., 2018; Kilgore et al., 2018), or to deserpentinization (Evans and Frost, 2021). The redox budget (Evans, 2006, 2012; Evans and Tomkins, 2011, Malaspina et al., 2009, 2017) of subducted slab-derived fluids could change the redox state of the mantle wedge by transporting such redox sensitive elements as iron, carbon and sulfur into it (Rielli et al., 2017; Bénard et al., 2018; Debret et al., 2020). Generally, the fO_2 of the mantle wedge is higher than that of the oceanic mantle (Malaspina et al., 2009; Evans et al., 2012, 2017; this study).

In this study, I contribute new mineralogical and fO_2 information to constrain redox conditions in the Fe-Ni-Co-O-S system and the role of hydrothermal processes in upgrading magmatic sulfide tenors, desulfurization (sulfur-loss) of magmatic pentlandite and hydrothermal

upgrading of the sulfide phases in Abu Dahr forearc environment. Then, I correlate these data with those from global Ni–rich serpentinites.

The redox conditions, expressed in terms of fO_2 and fS_2, are controlled by the mineralogy and stabilities of Ni-rich phases in serpentinization environments (Frost, 1985; Klein and Bach, 2009; Schwarzenbach et al., 2014, 2021; Foustoukos et al., 2015; de Obeso and Kelemen, 2020). In subduction zones, slab-derived fluids migrate upwards and cause serpentinization of the adjacent mantle wedge and subsequent partial melting (Zheng et al., 2020). The products of serpentinization depend on the primary mineralogy of the protolith, water/rock ratios, temperature, pressure and fluid composition (e.g. Frost, 1985; Frost and Beard, 2007; Schwarzenbach et al., 2014). Variations in water/rock ratios lead to strong variations in fO_2 and fS_2 conditions (Frost, 1985; Bach et al., 2006; Delacour et al., 2008; Ishimaru et al., 2009; Klein and Bach, 2009; Frost et al., 2013; Schwarzenbach et al., 2014; Evans et al., 2017; de Obeso and Kelemen, 2020). Serpentinization at low water/rock ratios commonly leads to lower fO_2 and fS_2 and favors the formation of low-sulfur sulfide assemblage of heazlewoodite, Fe-Ni alloys (e.g., taenite, awaruite), native metals, magnetite and hydrogen (Frost, 1985; Alt and Shanks, 1998, 2003; Delacour et al., 2008). In contrast, serpentinization at higher water-rock ratios leads to higher fO_2 with an assemblage of millerite, pyrite, hematite and sulfate (Frost, 1985; Alt and Shanks, 1998, 2003; Delacour et al., 2008). The sulfide mineral assemblages provide constraints on fO_2 and fS_2 prevailing during hydrothermal alteration (Alt and Shanks, 1998, 2003; Delacour et al., 2008 Schwarzenbach et al., 2012, 2014, 2021).

This study has documented for the first time the presence of a variety of Ni-rich Ni-Fe (-Co) sulfide and metal phases along with Fe-oxides/oxyhydroxides in serpentinized-carbonated peridotites of Abu Dahr forearc. The main goals of this study are to: 1) describe the mineralogy,

mineral assemblages and textures of the high-Ni sulfide and intermetallic minerals in Abu Dahr as potentially major Ni suppliers for Ni resource exploration, compared with other Ni-rich serpentinites worldwide; 2) identify the paragenetic sequence of the Ni-rich phases based on mineral textures and associations; 3) determine the composition of the Ni-rich phases and their relationship to fO_2 and fS_2 conditions; and 4) discuss the role of hydrothermal processes in upgrading disseminated magmatic sulfide tenors, desulfurization of magmatic sulfides and secondary upgrading of the sulfide phases, and their reflection on the magmatic and post-magmatic evolution of the Abu Dahr complex.

Geological Setting and Samples

The Abu Dahr area (23º 30′-23º 40′ N, 35º 00′-35º 10′ E, Fig. 1) is located in the South Eastern Desert of Egypt, ~70 km NW of Shalatin city on the Red Sea, and covers the largest part of Beitan province. It forms a part of the Arabo-Nubian Shield (890-570 Ma, Stern et al., 2004) and comprises Neoproterozoic Beitan gneisses, dismembered ophiolite, island arc metavolcanic-plutonic assemblage, volcaniclastic metasediments (mélange matrix), and syn-to late-tectonic granite intrusions (Ashmawy, 1987; Abdel-Khalek et al., 1992; El Tahlawi et al., 1997; Zoheir et al., 2008; Khedr and Arai, 2013, 2016; Gahlan et al., 2015; Abdel-Halim et al., 2020; Khedr et al., 2022). According to field relationships, the following sequence was established by El Tahlawi et al. (1997) starting with the uppermost rock unit: 1) Abu Dahr Nappe, 2) Arayis ophiolitic mélange, 3) Egat metavolcaniclastics, and 4) Beitan gneisses. The Abu Dahr ophiolite consists, from the base upward, of a mantle section (Abu Dahr Peridotite Nappe), ultramafic-mafic cumulates, and crustal metagabbros and metabasalts (Gahlan et al., 2015; Abdel-Halim et al., 2020; Khedr et al., 2022). The crustal rocks are associated with the Arais and Balamhindit ophiolite complexes (Khedr and Arai, 2013, 2016).

The Peridotite Nappe of Abu Dahr (~150 km^2) is the second largest, well–exposed and preserved Neoproterozoic ultramafic rocks (after El Gerf) in the South Eastern Desert, Egypt. The Abu Dahr Nappe is composed mainly of highly depleted clinopyroxene-poor harzburgites with minor dunites (+ chromitites) and pyroxenites. The nappe, structurally, forms the uppermost lithotectonic unit, thrusted southwestwards onto Beitan gneisses. It is divided into two major domains separated by EW-trending Abu Khayl fracture zone: Abu Dahr North and South (Abdel-Halim et al., 2020). The Abu Dahr North consists of harzburgite with minor dunite (+ chromitite), cut by a network of olivine–orthopyroxenite dykes. The harzburgites are partially serpentinized to form lizardite-bearing serpentinites (Lz-serpentinites), but pristine harzburgites are more abundant at Wadi Abu Mastoura (~4 km long). The chromitites are massive to disseminated high-Cr chromitites composed of magnesio-chromite with high Cr# values (83-93) containing inclusions of platinum-group minerals (PGM) + base-metal sulfides (BMS) + Au (Abdel-Halim et al., 2020). Massive chromitites form large pods within dunite 'envelopes' in harzburgites host. Magnesite veins (up to 1 m wide) are common in the serpentinized harzburgites. Gabbroic and doleritic dykes are also encountered. Antigorite serpentinites (Atg-serpentinites) constituting Abu Dahr South were transformed to carbonate-rich serpentinites (listvenites) along fractured and sheared zones. The Abu Dahr Nappe is intruded by concentric intrusive complexes of Um Eliega and Rahaba from the north and east, respectively (Zoheir et al., 2008; Abdel-Karim et al., 2021; Azer and Asimow, 2021). These complexes consisting of a mafic core (gabbro and diorite) surrounded by tonalite in the middle to granodiorite at the margin, formed in an active continental margin setting during the subduction of the oceanic slab (Abdel-Karim et al., 2021).

The samples studied were collected from surface outcrops of northern and southern Abu Dahr. The sample localities are shown in Figure 1 and their coordinates are listed in Table 1. The samples include harzburgites, dunites, chromitites, and orthopyroxenites. The harzburgites considered here, are partially to completely serpentinized.

Analytical Methods and Calculations of P-T and fO_2

More than 200 polished thin sections (PTS) were investigated at various magnifications (100 and 200X) using dual-purpose optical microscope incorporating both transmitted- and reflected-light options and scanning electron microscope (SEM) hosted in the Department of Geology at Assiut University, Egypt. The modal abundances of sulfides were determined by point counting technique at 500X magnification.

The mineral chemistry of Ni-sulfides, metal alloys, olivines, pyroxenes, amphiboles, Cr-spinels and Fe-oxides/oxyhydroxides was determined by Electron Microprobe (EMP) analysis using a JEOL (JSM-6310) instrument by wavelength dispersion spectroscopy (WDS) and energy dispersive spectroscopy (EDX) at the Institute of Earth Sciences, Karl Franz University, Graz, Austria. Operating conditions of the electron beam were 20 kV accelerating potential, 20 nA beam current, 1 μm beam diameter, and 10 s measurement time (peak) for Cu, Co, Fe, Mg, Ni, O, S and Si. Natural and synthetic silicate and oxide standards were used for calibration. Silicate standards were quartz for Si, titanite for Ca and Ti, synthetic corundum for Al, garnet for Fe, olivine for Mg, jadeite for Na, adularia for K, chromite for Cr, rhodonit for Mn, and nickel oxide for Ni. Standards for base-metal minerals were chalcopyrite for S, Fe, and Cu; cobalt for Co; nickel for Ni; silver for Ag; Cabri-141 (NiSb) for Sb; and Cabri-526 (PtAs2) for As. The relative analytical error is better than 1% (1σ) except for element contents < 1 wt%, where the analytical error is better than 4% (1σ).

Major- and trace-element contents of bulk-rocks were determined by X-ray fluorescence spectrometry (XRF) and inductively coupled plasma mass spectrometry (ICP-MS) at the Institute of Earth Sciences, Karl Franz University, Graz, Austria. Major elements were determined by XRF using fused glass disks, excited with X-ray radiation, normally generated by an X-ray tube operated at a potential of between 10 and 100 kV, with relative precision of < 1%.. The analytical error is less than 0.6 wt% for all major elements. Loss on ignition (LOI) was calculated after heating the powdered samples at 1050ºC for 2 hours. Trace-element concentrations were measured by ICP-MS using an Agilent 7500 s quadrupole ICP-MS system attached to a New Wave/Merchantek UP213 laser ablation system. The analyses were carried out with a beam diameter of 15 μm and a 5 Hz repetition rate. Helium was used as carrier gas and N_2 was added to optimize the detection limits. The energy density was 4 J/cm^2, and the repetition rate was set at 6 Hz. Quantitative results were obtained through calibration of relative element sensitivities using the NIST-610 standard glass. The analytical error is less than 0.1 ppm by weight for most elements.

Calculations of P-T and fO_2. Equilibration temperatures for the studied harzburgites were determined using the two-pyroxene thermometers (Wood and Banno, 1973; Wells, 1977; Brey and Köhler, 1990) and Ca-in-orthopyroxene thermometer of Brey and Köhler (1990). The two-pyroxene geobarometer suggested by Putirka (2008) was used to determine the pressure conditions under which the peridotites could have formed. The fO_2 of the Abu Dahr harzburgites was determined using the oxybarometry of Ballhaus et al. (1991) based on spinel-olivine-orthopyroxene oxybarometry equilibrium at a pressure of 1 GPa, which is approximately the center of the spinel stability field (see Fig. 13 of Simon et al., 2008; Dare et al., 2009; Birner et

al., 2016), and adopted Tk from the equilibrium temperatures of Brey and Köhler (1990) in fO_2 calculations.

The fO_2 of peridotites can be calculated using phase equilibrium between olivine (Ol), orthopyroxene (Opx), and spinel (Spl) (R1):

$$6Fe_2SiO_4\ (Ol) + O_2 = 3Fe_2Si_2O_6\ (Opx) + 2Fe_3O_4\ (Spl) \quad (1)$$

The calculation of fO_2 depends on the pressure and temperature of equilibrium. For this study, we used the two-pyroxene thermometers (Wood and Banno, 1973; Wells, 1977; Brey and Köhler, 1990) and Ca-in-orthopyroxene thermometer of Brey and Köhler (1990). The fO_2 values are calculated relative to the fayalite-magnetite-quartz (FMQ) buffer in log units using the olivine-spinel oxybarometry of Ballhaus et al. (1991) and the formula of them assuming a pressure of 1 GPa as follows (R2):

$$\Delta\log (fO_2)^{FMQ} = 0.27 + 2505/T\text{-}400P/T\text{-}6 \log (XFe^{Ol})\text{-}3200(1\text{-}XFe^{Ol})^2/T + 21\text{og} (XFe^{2+Spl}) + 4 \log (XFe^{3+Spl}) + 2630\ (XAl^{Spl})^2/T \quad (2)$$

The uncertainty in the calculated fO_2 originates from analytical errors and errors associated with activity estimates of components in Eq. (1). Analytical errors in silicate compositions contribute little to the fO_2 uncertainty. For example, olivine composition has an error of less than ±0.003 in XFe, which translates into an uncertainty of ±0.15 log units in fO_2. Orthopyroxene grains are more heterogeneous in composition than olivine in individual samples; however, propagated uncertainties from this heterogeneity are also small, on the order of 0.1 log units in fO_2 or less. Inaccurate Fe^{3+} contents in spinel are the major cause of error in calculated fO_2. The oxygen fugacity recorded by mantle minerals is unaffected by nearby low-temperature serpentinization, and is representative of mantle processes (Birner et al., 2016).

Results

Peridotite petrography

The harzburgites show a wide range of serpentinization from 0% to 100%, and exhibit a sequence of hydrothermal alteration from harzburgites → Lz-serpentinites → Atg-serpentinites → Atg-talc-magnesite → quartz-carbonate listvenites. Figure 2 shows the paragenetic sequence for Abu Dahr ophiolitic rocks and associated silicates, carbonates, oxides, and Ni-sulfides and metal alloys. The fresh harzburgites show a typical porphyroclastic texture, characterized by millimeter-sized forsterite-rich olivine (Mg# is 91-93), orthopyroxene with lesser amounts of clinopyroxene lamellae (< 1 vol.%), and Cr-spinel, as well as Ca-amphiboles (magnesio-hornblende and tschermakite). Orthopyroxene porphyroclasts are surrounded by domains of polygonal or irregularly shaped olivine neoblasts (Fig. 3a, b). Lz-serpentinites from Abu Dahr North are primarily composed of low temperature serpentine (*i.e.* lizardite and/or chrysotile) forming mesh and bastite textures after olivine and orthopyroxene, respectively, with disseminated magnetite and interstitial sulfides (Fig. 3c, d). Brucite is developed in the centers of narrow serpentine veinlets, and occurs as thin veins associated with serpentine and/or magnetite (Fig. 3d), similar to brucite texture from Santa Elena (see Fig. 8 of Schwarzenbach et al., 2016) and Mariana (see Fig. 2 of Albers et al. 2020). Cr-spinel is virtually unaltered but some grains exhibit variably thick ferritchromite rims. Atg-serpentinites from Abu Dahr South consist of ~100% antigorite with an interlocking texture, minor carbonate (magnesite and dolomite), Fe-oxides/oxyhydroxides, talc, and Ni-sulfides and Ni-rich awaruite (Fig. 3e). Well-zoned chromites with ferritchromite and nickeliferous magnetite rims are widely distributed in samples from both areas (Fig. 3f).

Disseminated Ni mineralization of Abu Dahr

Primary sulfides

The major sulfides of mantle rocks, pentlandite, pyrrhotite, and chalcopyrite are present in low abundance and occur interstitially amongst the silicates (e.g., Harvey et al., 2016; Lorand and Luguet, 2016; Kiseeva et al., 2017; Vaughan and Corkhill, 2017). At Abu Dahr, pentlandite $(Fe,Ni,Co)_9S_8$, the dominant primary mantle sulfide mineral, occurs as single mineral grains (pentlandite/cobaltian pentlandite) from 10 to 2,000 μm in size (Fig. 4a, e), and/or as composite intergrowth (10-50 μm across) of pentlandite and its replacement secondary phases (Figs. 5a, b, 5a). Chalcopyrite is a rare mineral; other Cu-phases, Fe-sulfides and Ni-arsenides/phosphides are not present in the investigated samples.

Mineral assemblages

In Abu Dahr serpentinized peridotites, a variety of high-Ni sulfide and metal phases occur, including high-Ni pentlandite, cobaltian pentlandite, heazlewoodite, godlevskite, millerite, awaruite, and native Ni along with magnetite and goethite. The mineral abbreviations (after Whitney and Evans, 2010) and stoichiometric formulas of the primary and secondary sulfides and metals mentioned in the text are given in Table 2. The Ni-sulfide and metal alloy minerals are disseminated in every polished thin section, and display low abundance (<< 1% of the bulk rock; Kiseeva et al., 2017). Based on the dominant Ni-bearing sulfide mineral, sulfide assemblages are divided into three distinct facies: (1) pentlandite-rich; (2) godlevskite-rich; and (3) millerite-rich. Magnetite is present in almost all assemblages as fine-grained disseminations in serpentinites.. Typical assemblages and intergrowths are illustrated in Figures 4-6.

Pentlandite-rich assemblages. Pentlandite-awaruite-magnetite and cobaltian pentlandite-heazlewoodite-magnetite are the dominant assemblages (Fig. 4a-f) in partially serpentinized peridotites (lizarditization stage).

Godlevskite-rich assemblages. Cobaltian pentlandite-heazlewoodite-godlevskite-magnetite and heazlewoodite-godlevskite-magnetite are the main mineral assemblages (Fig. 5a-d) in fully serpentinized rocks (antigorite stage).

Millerite-rich assemblages. Cobaltian pentlandite-heazlewoodite-millerite and millerite-native Ni-goethite assemblages are the major Ni-sulfide/native Ni/Fe-oxyhydroxide minerals of the carbonation stage (Fig. 6a, b) in steatized (talc-carbonated) serpentinites (carbonation stage).

Replacement textures of Ni-rich phases

Based on their textural relations, primary pentlandite occurs as finely disseminated discrete grains of Ni-rich pentlandite/cobaltian pentlandite (less than 20 μm) associated with the serpentine matrix (Fig. 4a), or in rare cases as euhedral grains of pentlandite replaced by heazlewoodite (Fig. 4b). Awaruite occurs as finely disseminated euhedral grains (< 10 μm) of Ni-rich awaruite (native Ni) core rimmed by stoichiometric awaruite (Fig. 4c) and as interstitial disseminations (> 2 mm) of desulfurized pentlandite (Fig. 4d-f). Heazlewoodite commonly replaces cobaltian pentlandite forming composite intergrowths of cobaltian pentlandite-heazlewoodite (Fig. 6a). In fully serpentinized rocks, godlevskite replaces heazlewoodite forming composite intergrowths of cobaltian pentlandite-heazlewoodite-godlevskite (Fig. 5a), cobaltian pentlandite-heazlewoodite-godlevskite-magnetite (Fig. 5b), and heazlewoodite-godlevskite (Fig. 5c). Magnetite commonly mantles heazlewoodite and godlevskite (Fig. 5d). Heazlewoodite co-occurring with godlevskite may also contain small cobaltian pentlandite inclusions, which are lacking in godlevskite. This indicates that godlevskite did not directly grow

at the expense of cobaltian pentlandite; it is more likely that godlevskite replaces heazlewoodite in fully serpentinized rocks. Pentlandite is also replaced by secondary magnetite forming the sulfide-magnetite composite grains (Fig. 5b).

With increasing the degree of steatitization (carbonation), low-sulfur Ni-sulfides are progressively replaced by sulfur-rich Ni-sulfides. Millerite grows at the expense of the low-sulfur heazlewoodite and godlevskite (Figs. 4f, 6a). Godlevskite is replaced by a reticulate pattern of lamellar millerite veinlets of ~ 5 μm width (Fig. 4f). Millerite in these veinlets is fibrous in habit and appears to follow structural directions in the replaced godlevskite (Hudson and Travis, 1981). The completely steatized rocks contain rounded and irregular grains of millerite (Fig. 6b). The Ni–rich awaruite (native Ni) rims the millerite grain boundaries (Fig. 6b). Euhedral tabular goethite crystals occur in association with millerite and forms rims on millerite (Fig. 6b). These textural patterns occur as a result of sulfide replacement processes (Rottier et al., 2016). Chalcopyrite ($CuFeS_2$) is not present and rarely occurs as small supergene grains intergrown with the millerite-rich assemblage (Fig. 6a).

Paragenesis

The paragenetic sequence of the Ni-bearing phases of Abu Dahr peridotites accompanying the serpentinization and carbonation processes is summarized in Figure 2. Textural relationships suggest this generalized paragenetic sequence: Pentlandite → cobaltian pentlandite → awaruite/native Ni (and/or heazlewoodite), and heazlewoodite → godlevskite → millerite, and awaruite → millerite and goethite. This sequence is consistent with the desulfidation during initial serpentinization; progressive serpentinization allows the formation of high-sulfur assemblages. On the basis of predominant minerals, mineral textures and associations, there were four main stages of formation and modification of Ni-bearing minerals: stage (1) involved

replacement of orthomagmatic pentlandite/cobaltian pentlandite by awaruite and/or heazlewoodite; stage (2) replacement of heazlewoodite by godlevskite; stage (3) replacement of godlevskite by millerite; and stage (4) Ni-rich awaruite broke down to millerite and goethite.

Although pyrrhotite occurs in many serpentinized peridotites described in the literature (e.g. Shiga, 1987; Abrajano and Pasteris, 1989; Lorand, 1989; Miller, 2007), it is absent in all the investigated samples from Abu Dahr. Even the pyrrhotite was present, and based on other case studies, the formation of magnetite decreases the Fe:Ni ratio of the sulfides, increasing the ratio of Ni-bearing sulfides to Fe-bearing sulfides (pyrrhotite), until pyrrhotite disappears. This also explains that the mineral pyrrhotite may be occurred, but disappears with progressive serpentinization and magnetite formation.

Mineral chemistry

Primary mantle assemblage

Primary mineral compositions of Abu Dahr harzburgites are reported in Table S1 (supplementary material). Olivine in the harzburgites has forsterite (Fo) values of 91-93 (average = 92). Their NiO and MnO contents are in the range of 0.36-0.57 wt% (corresponding to 2828-4478 ppm Ni) and 0.02-0.3 wt%, respectively. Spinel Cr# (=100 Cr/Cr + Al) values range from 55 to 65 (av. 62) and Mg# (=100 Mg/Mg + Fe) from 53 to 57. The compositional plots of spinel Cr# versus olivine Fo and spinel Cr# versus Mg# are illustrated on Figure 7a and b. Orthopyroxene is enstatite with high Mg#, which ranges from 91.7 to 92.3 (average = 92). Clinopyroxene (exsolution lamellae in the orthopyroxene) is diopside with Mg# ranging from 94.1 to 95.2. Primary amphiboles of the Abu Dahr harzburgite are magnesio-hornblende (Mg# 94-97) and tschermakite (Mg# 78-80) of the calcic-amphibole group.

Ni-rich sulfide and alloy phases

Pentlandite and cobaltian pentlandite. Pentlandite is the dominant sulfide mineral at Abu Dahr and shows stoichiometric compositions ranging from $(Fe_{3.86}Ni_{4.85}Co_{0.29})_9S_8$ to $(Fe_{3.72}Ni_{4.99}Co_{0.29})_9S_8$ (Table 3). All of the pentlandite grains analyzed (13 grains) contain between 26.06-27.95 (average = 27.13 ± 0.91) wt% Fe, 34.58-36.69 (average = 35.79 ± 1.04) wt% Ni, and 1.59-2.72 (average = 2.10 ± 0.47) wt% Co (Table 3, Fig. 8a). In this study, pentlandite has a high-Ni tenor (up to 5.00 apfu (atoms per formula unit) Ni), with Ni/Fe ratios ranging from 1.18 to1.34 (average = 1.26 ± 0.07). The atomic metal/sulfur ratios displayed by the Abu Dahr pentlandites are 1.01-1.08 (average = 1.04 ± 0.03). Pentlandite contains up to 2.72 wt% Co, and the Ni/Co ratio is 13.0-23.2 (average = 17.79 ± 4.16). In the ternary system Fe_9S_8-Ni_9S_8-Co_9S_8 (Kaneda et al., 1986), the Abu Dahr pentlandites plot within the pentlandite stability field at 200°C (Fig. 8b).

The average cobaltian pentlandite composition is $(Fe_{3.47}Ni_{4.78}Co_{0.75})_9S_8$ Co with average values of 24.76 ± 1.24 wt% Fe, 35.81 ± 0.79 wt% Ni, and 5.64 ± 0.86 wt% Co (Table 3, Fig. 8a). The Ni/Fe ratios are 1.28-1.54 (high-Ni). The atomic metal/sulfur ratios (1.03-1.16) are consistent with those of pentlandite. The cobaltian pentlandite is characterized by, remarkably, high Co contents of 5.00 to 7.53 (average = 5.64) wt% Co with Ni/Co ratios (4.82-7.23, average = 6.48 ± 0.83) typical of mantle sulfides worldwide (Wang et al., 2010). Binary plots (Fig. 9a-d) were generated to compare the Abu Dahr pentlandites with sulfides from forearc mantle wedge settings worldwide (e.g., Vourinos, Greece: Tzamos et al., 2016; Massif du Sud Peridotite Nappe, New Caledonia: Augé et al. 1999; Cemetery Ridge, Arizona: Haxel et al., 2018; Santa Elena Nappe, Costa Rica: Schwarzenbach et al., 2014; Latao, SE Sulawesi: Rafianto et al., 2012). The Abu Dahr pentlandites display a positive correlation between Co and Ni (Fig. 9a) and

negative correlation between Fe and Fe + Ni (Fig. 9b, c). Similarly, Fe shows a strong negative correlation with Co+Ni (Fig. 9d), similar to typical mantle wedge occurrences worldwide.

Heazlewoodite. The average composition of analyzed heazlewoodite is $(Fe_{0.07}Ni_{2.93})_3S_2$ with 1.57 ± 1.54 wt% Fe, 70.86 ± 1.13 wt% Ni (2.93 apfu Ni) and no detectable Co (Table 4, Fig. 8a). The atomic metal/sulfur ratio of heazlewoodite ranges from 1.32 to 1.54 (average = 1.44 ± 0.07), with lower values where heazlewoodite replaces cobaltian pentlandite (1.32), and slightly elevated values when heazlewoodite is associated with godlevskite-rich assemblages. Heazlewoodite contains variable amounts of Fe (0.39-3.78 wt%); heazlewoodite associated with relict cobaltian pentlandite is Fe-poor (0.41-1.87 wt%), and Fe-rich where it is associated with or mantled by magnetite (3.60-3.78 wt%).

Godlevskite. The average composition of godlevskite is $(Fe_{0.26}Ni_{8.73}Co_{0.01})_9S_8$ with average concentrations of 1.92 ± 0.55 wt% Fe and 67.48 ± 0.86 wt% Ni) (8.73 apfu Ni) (Table 4, Fig. 8a). The atomic metal/sulfur ratio of godlevskite ranges from 1.21 to 1.29 (average = 1.25). The average ratio is higher than the theoretical value of 1.125. Metal/sulfur ratios are slightly higher where godlevskite replaces heazlewoodite (1.27-1.29), and lower where godlevskite coexists with cobaltian pentlandite (1.21-1.22). The Fe and Co contents of godlevskite (2.33, 0.20 wt%, respectively) are elevated when godlevskite is associated with relict cobaltian pentlandite.

Millerite. The average composition of millerite is $(Fe_{0.01}Ni_{0.98}Cu_{0.01})S$. Average element concentrations are 0.65 ± 0.19 wt% Fe, 64.67 ± 0.75 wt% Ni (0.98 apfu Ni), 0.13 ± 0.16 wt% Co, and 0.39 ± 0.72 wt% Cu (Table 4, Fig. 8a). The atomic metal/sulfur ratio of millerite ranges from 0.95 and 1.10 (average = 1.02 ± 0.06), with slightly elevated values of 1.10 (average = 1.09) where millerite replaces heazlewoodite. Millerite associated with native Ni shows elevated Fe contents (up to 0.83 wt% Fe, with no Co or Cu). The Fe content also increases when millerite

is associated with relict cobaltian pentlandite-heazlewoodite-chalcopyrite (0.85 wt%), and the Co and Cu contents of this millerite are up to 0.35 wt% and 1.79 wt%, respectively.

Chalcopyrite. The average composition of chalcopyrite is $(Fe_{0.98}Cu_{0.98}Ni_{0.05})_2S_2$. The element concentrations are 29.60 wt% Fe, 33.67 wt% Cu, and 1.49 wt% Ni, with no detectable Co (Table 4, Fig. 8a).

Awaruite and native Ni. Awaruite exhibits a wide compositional range from $Ni_{75}Fe_{21}$ (stoichiometric Ni_3Fe) to $Ni_{93}Fe_5$ (native Ni) (Table 4, Fig. 8a); only a few analyses are classified as awaruite *sensu stricto* (Ni_3Fe). Euhedral awaruite shows Ni zonation, with a stoichiometric awaruite rim of 21.76 wt% Fe and 76.41 wt% Ni and Ni-rich core containing 13.47 wt% Fe and 85.03 wt% Ni. Co is present in minor amounts of less than 1.15 wt%. Native nickel grains have Ni contents of 91.7 to 93.0 wt% (average = 92.20 ± 0.49), with variable Fe contents (4.96-6.28 wt%, average = 5.58 ± 0.78) and minor Co and Cu contents (0.43 ± 0.11 and 1.78 ± 0.38 wt%, respectively).

Fe–oxides/oxyhydroxides

Nickeliferous magnetite and goethite. The Cr-spinel alteration phases (ferritchromite and magnetite) and goethite from Abu Dahr are enriched in Ni (Table 5); however, primary chromites are Ni-free (Table S1 (supplementary material). Ferritchromite has relatively high Ni contents (0.24-1.19, average = 0.63 wt% NiO). Magnetite rims to ferritchromite have the highest Ni contents (0.40-1.24, average = 0.75 wt% NiO, Table 5), than the serpentinization-related magnetite from the Dumont sill, which contains average 0.07 wt% NiO (Sciortino et al., 2015). Magnetite intergrown with pentlandite-heazlewoodite-godlevskite (Fig. 5b) has not yet been analyzed. The nickeliferous goethite (Fe, Ni)O(OH) has Ni concentrations of 1.91 to 2.12 (average = 2.02) wt% NiO (Table 5).

Equilibrium P-T and oxygen fugacity calculations

The results of calculated P-T and the fO_2 values (expressed as the deviation from FMQ in log units, $\Delta\log(fO_2)$FMQ (fayalite-magnetite-quartz)) for Abu Dahr harzburgites are given in Table 6.

The equilibrium temperatures estimated using the Brey and Köhler (1990) Ca-in-orthopyroxene and two-pyroxene thermometers, suggest that the Abu Dahr harzburgites equilibrated at temperatures of 910-1217°C. Equilibration pressures using two-pyroxene geobarometer of Putirka (2008) gave pressure values between 4.1 and 7.8 kbar (0.4-0.8 GPa). The calculated fO_2 values for Abu Dahr harzburgites range from FMQ +0.41 to FMQ +1.20 and correlated positively with melting (spinel Cr#) (Fig. 7c).

Whole-rock geochemistry

The results of whole rock major and trace element analyses of 5 samples from Abu Dahr are reported in Table 7. Bulk-rock geochemistry is strongly affected by hydrothermal alteration, consistent with findings from subduction-related and abyssal serpentinites worldwide (e.g. Deschamps et al., 2010; Marchesi et al., 2013; Uno and Kirby, 2019), and the high loss on ignition (LOI) values 9.22-12.71 wt% indicate the presence of H_2O and CO_2 (serpentine, brucite, magnesite). Major elements are normalized to 100% anhydrous compositions, with Mg# values and total FeO of most of the harzburgites falling within a restricted range (89-91 and 8.71-10.54 wt%, respectively). The MgO and SiO_2 contents are variable (41.24-46.83 and 42.12-46.92 wt%, respectively), consistent with increased depletion of the harzburgites. These samples have low concentrations of Al_2O_3 (0.41-0.90 wt%) and TiO_2 (0.01-0.06 wt%) indicating a highly depleted

nature, which is consistent with a highly refractory mantle residue after high-degree partial melting (Pearce et al., 2000). The CaO contents are generally low (0.20-0.34 wt%) reflecting the scarcity of clinopyroxene in the peridotites, but two samples (322/3 and 324/4) have relatively high 1.83 and 1.49 wt% CaO. The MgO values can be used effectively as an indicator of the degree of depletion. Any increase in the MgO content is consistent with increased depletion and higher olivine contents (Wu et al., 2017). On Harker diagrams (Fig. 10a-d), the Abu Dahr harzburgite samples show relatively linear decreases in SiO_2, Al_2O_3 and CaO contents with increasing MgO, but total FeO increases slightly with increasing MgO. These trends indicate the depleted nature of Abu Dahr peridotites and are similar to those of ultramafic rocks from similar settings (e.g., Mariana forearc: Parkinson and Pearce, 1998; Cemetery Ridge, Arizona: Haxel et al., 2018; Santa Elena Nappe, Costa Rica: Schwarzenbach et al., 2014). All samples are significantly depleted relative to the primitive mantle (Fig. 10a-d).

Trace element analyses show that the serpentinized harzburgites of Abu Dahr are enriched in Cr (2461-7849 ppm), Ni (1489-2590 ppm) and Co (119-144 ppm) relative to fresh harzburgites of northern Abu Dahr. In contrast, the analyzed samples are notably depleted in Cu (0.1-10.9 ppm), below the average Cu concentration in spinel harzburgites 35±11 ppm (Ciazela et al., 2015). The Abu Dahr harzburgites exhibit very low concentrations of the incompatible trace elements (Zn, Sc, V and Y), LILE (K, Rb, Ce, Sr, Ba) and HFSE (Zr, Y, Nb, Hf, Ta, U); reflecting the highly residual nature of the peridotites and their low clinopyroxene content (< 1.0 vol%). The rare-earth element (REE) contents are also very low.

Discussion

Based on the textural evolution of Ni–bearing phases and their mineralogical and chemical composition data, the important aspects to be discussed here are the relationship between redox

state (changes in fO_2 and fS_2) and Fe-Ni-Co-O-S minerals. In the following, we will first discuss the petrogenesis, oxidation state, and serpentinization of Abu Dahr harzburgites; and then discuss: (1) Remobilization of Ni from magmatic olivines and upgrading of magmatic sulfide tenor; (2) Relationship between redox state and Fe-Ni-Co-O-S minerals; (3) High Co contents of pentlandite in Abu Dahr; (4) Similarities to Ni-sulfides and alloys from forearc mantle elsewhere; and finally (5) Genetic model for Abu Dahr Ni-sulfides and metal alloys.

Petrogenesis of the Abu Dahr protolith

Peridotites of Abu Dahr are mainly highly depleted clinopyroxene-poor harzburgites with forsterite-rich olivine (Fo 91-93) and high Cr# spinel (55-65, average = 62), and are similar to harzburgites from other areas of the ophiolites in the Eastern Desert (e.g., Azer and Stern 2007; Khedr and Arai, 2013, 2016). Spinel cores chemistry is extensively used as a petrogenetic (Dick and Bullen, 1984; Arai, 1992, 1994; Hellebrand et al., 2001) and tectonic setting (Arai, 1992; Dare et al., 2009) indicator in ultramafic and mafic rocks. Based on olivine and spinel chemistry, the compositional plots of spinel Cr# versus coexisting olivine Mg# and spinel Mg# versus Cr# have shown that the Abu Dahr harzburgites are residues of high-degrees of partial melting (~ 35%), plotted within the field of forearc peridotites and on modern Mariana forearc peridotite field (Fig. 7a, b). On the tectonic discrimination diagram of fO_2 versus spinel Cr# (Dare et al., 2009), the Abu Dahr harzburgites plotted within the field of SSZ harzburgites (Fig. 7c).

Oxidation state of the Abu Dahr forearc

The spinel-olivine-orthopyroxene oxybarometry of Ballhaus et al. (1991) was used to estimate the oxidation state of Abu Dahr forearc peridotites, assuming a 1 GPa equilibrium pressure. The calculated fO_2 values for Abu Dahr forearc peridotites range from FMQ +0.41 to FMQ +1.20 (average = +0.60 FMQ), fall within the range from FMQ +0.3 to FMQ +2 of forearc mantle

wedge (Parkinson and Arculus, 1999), and are within the ±2 FMQ of the upper mantle (Frost and McCammon, 2008). The calculated fO_2 is positively correlated with spinel Cr# (Fig. 7c), indicating that higher melting degrees may influence the oxidation state of the mantle wedge, as demonstrated in previous studies (Parkinson and Arculus, 1999; Kelley and Cottrell, 2009; Kilgore et al., 2018).

The oxidation state of the Abu Dahr forearc harzburgites (+0.41 to +1.20 FMQ) is in agreement with the previous studies, which concluded that the mantle wedge is generally more oxidized than oceanic mantle (e.g., Ballhaus, 1993; Parkinson and Arculus, 1999; Arai and Ishimaru, 2007; Malaspina et al., 2009; Evans et al., 2012 (FMQ 1-4); Bénard et al., 2018 (FMQ +0.5 to +1.5); Kilgore et al., 2018; Wang et al., 2020), and subcontinental lithospheric mantle (Perinelli et al., 2012, FMQ -1.52 to -0.23).

Serpentinization of Abu Dahr peridotites

The Abu Dahr peridotites have experienced multiple stages of serpentinization (lizarditization and antigoritization) and carbonation/listvenitization. Lizardite-brucite-magnetite from olivine and bastites from pyroxene and amphibole characterize the lizarditization stage (T < 300°C; P < 4 kbar; depth < 13 km; lower aCO_2 and fO_2 and fS_2 (Pirajno, 2009; Schwartz et al., 2013; Debret et al., 2019; Boskabadi et al. 2020). Alteration of primary amphiboles is a Ca-releasing reaction and contributes to the Ca budget of the bulk peridotites. Alteration of olivine (R3 and R4) can be described in the following reactions (after Wang et al., 2009):

$$6(Mg, Fe)_2SiO_4 + 7H_2O = 3(Mg, Fe)_3Si_2O_5(OH)_4 + Fe_3O_4 + H_2(aq) \quad (3)$$

$$6(Mg, Fe)_2SiO_4 + 9H_2O = 3(Mg, Fe)_3Si_2O_5(OH)_4 + 3Mg_{0.8}Fe_{0.2}(OH)_2 \quad (4)$$

The alteration of amphibole releases aqueous Ca and SiO_2 (R5, after Wang et al., 2009):

$$Ca_2Mg_{4.8}Fe_{0.2}Si_8O_{22}(OH)_2 + 16/13H_2O + 38/13H^+ + 7/130Fe^{2+} =$$

$$24/13Mg_{2.6}Fe_{0.4}Si_2O_5(OH)_4 + 2Ca^{2+}(aq) + 56/13SiO_2(aq) \quad (5)$$

Magnetite formation is accompanied by release of iron from early formed phases such as Fe-serpentine R3 or Fe-brucite R6 (Bach et al., 2006; Frost and Beard, 2007; Wang et al., 2009; Frost et al., 2013; Boskabadi et al. 2020):

$$9Fe(OH)_2 + 4SiO_2(aq) = 2Fe_3Si_2O_5(OH)_4 + Fe_3O_4 + 4H_2O + H_2(aq) \quad (6)$$

The antigoritization stage is a high-temperature event (T > 320-410°C; P > 4 kbar; depth >13 km; higher aCO_2, $aSiO_2$, and fO_2 and fS_2 (Pirajno, 2009; Schwartz et al., 2013; Debret et al., 2019; Boskabadi et al. 2020) and is characterized by antigorite after lizardite in fully serpentinized samples. The onset of the carbonation stage occurred when infiltration of CO_2-rich fluids destabilized lizardite/chrysotile to form antigorite and Fe-magnesite (R7). More infiltration of CO_2-rich fluids destabilizes antigorite to form magnesite (R8) and talc (R9). Formation of antigorite-talc-magnesite rock is based on the following reactions (R7-R9, after Boskabadi et al. 2020):

$$17(Mg,Fe)_3Si_2O_5(OH)_4 + 3CO_3 = (Mg,Fe)_{48}Si_{34}O_{85}(OH)_{62} + 3Mg(Fe)CO_3 + 3H_2O \quad (7)$$

$$Mg_{48}Si_{34}O_{85}(OH)_{62} + 48CO_2(aq) = 48MgCO_3 + 34SiO_{2(aq)} + 31H_2O \quad (8)$$

$$Mg_{48}Si_{34}O_{85}(OH)_{62} + 30SiO_2(aq) = 16Mg_3Si_4O_{10}(OH)_2 + 15H_2O \quad (9)$$

The dehydration of Atg-serpentinites. Metamorphic olivine records external fluid infiltration during serpentinite dehydration (Clarke et al., 2020). Metamorphic olivine is formed during breakdown of brucite or antigorite (high-pressure serpentine) at ~400°C and ~650°C, respectively (Scambelluri et al., 2004). Partial dehydration (formation of prograde olivine at ~600˚C under high-pressure > 1 GPa) of Atg-serpentinites of Abu Dahr South occurs within

subduction channel. Antigorite, stable to 620°C at 1 GPa (Ulmer and Trommsdor, 1995), breaks down into metamorphic (secondary) olivine through antigorite dehydration during prograde metamorphism under high P-T conditions in subduction zones (Padron-Navarta et al., 2008; Debret et al., 2013; Deschamps et al., 2013). Antigorite commonly coexists with secondary olivine and clinopyroxene, suggesting high-temperature serpentinization at ~450-550°C (Murata et al., 2009). At Abu Dahr, the occurrence of secondary olivine and clinopyroxene (Fo 87 and Mg# 98, respectively, Table S1 (supplementary material) and talc in serpentinites suggests that the serpentinization and eclogitization took place under similar conditions (600°C, 20 kbar; Guillot et al., 2000). In areas with high hydrothermal alteration, serpentines have been transformed to fully carbonated peridotites (listvenites).

Remobilization of Ni from magmatic olivines and upgrading of magmatic sulfide tenor

Olivine is the main Ni-bearing mineral in the harzburgite and dunite protoliths and the major source of Ni forming the disseminated Ni mineralization (Marques et al., 2007; Kamenetsky et al., 2016). Partial melting of mantle peridotites increases the Ni contents of residual olivines (Herzberg et al., 2016). The high-Ni contents are consistent with high-Fo olivines (Sobolev et al., 2005, 2007; Nikkola et al., 2019). At Abu Dahr, harzburgite olivines are highly magnesian (Fo 91-93, average = 92) with higher NiO concentrations (0.33-0.57, average = 0.41 wt% NiO) than those reported from mantle wedge harzburgites worldwide (e.g., Mariana: 0.30-0.44 wt% NiO Wang et al., 2009; Himalaya: 0.38-0.39 wt% Hattori and Guillot, 2007; Tonga: 0.22-0.41 wt% Birner et al., 2017; Aladag: 0.31-0.51 wt% Lian et al., 2018; Oman: 0.38-0.39 wt% Negishi et al., 2013; New Caledonia: 0.30-0.41 wt% Secchiari et al., 2020).

At Abu Dahr, pentlandite is the dominant primary mantle sulfide mineral and has Ni tenor ranging up to 37 wt% (apfu Ni = 5). Serpentinization-related high-Ni tenor disseminated sulfide

deposits hosted within olivine-rich mantle peridotites are consistent with olivine compositions of Fo91-92 and attributed to release of Ni from magmatic olivine and enrichment of the tenor of pentlandite by Fe/Ni exchange between olivine and magmatic sulfides (R10, after Barnes et al., 2013):

$$FeS + NiO = FeO + NiS \quad (10)$$

Remobilization of Ni from magmatic olivines by postmagmatic fluids during serpentinization of Abu Dahr peridotites resulted in upgrading the Ni tenors of pre-existing primary pentlandite, explaining why Abu Dahr pentlandites have high Ni tenors and therefore, referred to here as high-Ni pentlandites (Table 3).

Relationship between redox conditions and Fe-Ni-Co-O-S minerals

In Abu Dahr, the redox conditions (changes in fO_2 and fS_2) recorded by Ni-rich phases are varying from highly reducing conditions during partial serpentinization stage to strongly oxidizing conditions during late stages of serpentinization and carbonation. Evidence thereof is that Abu Dahr exhibits three main Ni-rich assemblages: (1) pentlandite-rich assemblages (pentlandite-awaruite-magnetite and pentlandite-heazlewoodite-magnetite) in Lz-serpentinites; (2) godlevskite-rich assemblages (pentlandite-heazlewoodite-godlevskite-magnetite and heazlewoodite-godlevskite-magnetite) in Atg-serpentinites; and (3) millerite-rich assemblages (pentlandite-heazlewoodite-godlevskite-millerite and millerite-native Ni-goethite) in carbonated serpentinites. Similar redox conditions during serpentinization and talc-carbonation are recorded in the Fe-Ni-Co-O-S system (Eckstrand, 1975; Frost, 1985; Klein and Bach, 2009; Foustoukos et al., 2015; Sciortino et al., 2015; Evans et al., 2017), Cu-Fe-S-O-H system (Schwarzenbach et al., 2014, 2021), Fe-Ni-Cu-O-S system (de Obeso and Kelemen, 2020), and Ni-Fe-S-As minerals (González-Jiménez et al., 2021).

The phase diagram displayed in Figure 11 (modified after Frost, 1985) illustrates the phase stability in the Fe-Ni-Co-O-S minerals as a function of log fO_2 and log ΣS [a S_2(aq) + a SO_2(aq) + a H_2S(aq)] at 300°C and 2 KPa. In fact, fO_2 and fS_2 were not measured here (which is actually extremely difficult), but an assessment was made based on the comparison of existing parageneses with available diagrams (e.g., Frost, 1985). Therefore, Ni minerals in the Fe-Ni-Co-O-S system have been used here in a qualitative way to trace changes in fO_2 and fS_2 during serpentinization and carbonation (discussed below). In the following, I focused on (1) desulfurization (sulfur-loss) of magmatic pentlandite and formation of awaruite and magnetite, and (2) hydrothermal upgrading of Ni-rich sulfide phases.

Desulfurization (sulfur-loss) of magmatic pentlandite and awaruite formation. The assemblage pentlandite-awaruite-magnetite is linked to lizarditization of Abu Dahr forearc harzburgites; and commonly observed in partially serpentinized peridotites as the result of destabilization of pentlandite (Eckstrand 1975; Filippidis, 1985; Frost, 1985; Klein and Bach 2009; Schwarzenbach et al., 2014, 2021; Evans et al., 2017; Arai et al., 2020; González-Jiménez et al., 2021). High quantities of aqueous H_2 released during serpentinization produced a highly reducing and extremely low fO_2 and fS_2 environment which caused desulfurization (sulfur-loss) of pentlandite to form awaruite, magnetite, and aqueous H_2S according to the reaction (R11, Klein and Bach, 2009; Schwarzenbach et al., 2014, 2021):

$$Ni_{4.5}Fe_{4.5}S_8 + 4H_2(aq) + 4H_2O = 1.5Ni_3Fe + Fe_3O_4 + 8H_2S(aq) \quad (11)$$

A temperature of 200°C is suggested for the equilibration of pentlandite/cobaltian pentlandite from Abu Dahr based on its Co content (Fig. 8b; Kaneda et al., 1986). Previous work by Sciortino et al. (2015) and Olade (2019) has documented awaruite formed after primary sulfides with a narrow compositional range of approximately 70 to 75 wt% Ni, whereas Fe-Ni alloys

associated with serpentine, olivine, and magnetite show more compositional variation up to 100 wt% Ni. At Abu Dahr, nearly all Ni-Fe alloy awaruite exhibits a wide compositional range from 75 to 93 wt% Ni. Awaruite shows two forms: euhedral and anhedral. Euhedral awaruite embedded in serpentine (below 20 μm; Fig. 4c) may form by primary crystallization from a Ni-rich melt, upgraded to high-Ni awaruite (native Ni) up to 85 wt% Ni (the remaining Ni released from olivine during serpentinization). The solitary phase, euhedral microstructure, and characteristic compositional zonation with a stoichiometric awaruite rim (75 wt% Ni) and Ni-rich awaruite core (85 wt% Ni) indicate that awaruite was formed at higher temperatures from a Ni-rich melt. The most abundant awaruite grains are anhedral spherical usually formed by primary Ni-bearing sulfide pentlandite desulfurization (> 2 mm; Fig. 4d, e). Considering the P-T conditions estimated for initial serpentinization of the investigated Abu Dahr forearc (≤ 300°C and < 1 GPa), the association of awaruite and magnetite could be stable and in equilibrium with lizardite at log fO_2 ~ -41 to-38 and log ΣS < -2 (Fig. 11).

Partial dehydration of serpentinites and Ni-rich awaruite formation. Ni-rich awaruite or native nickel has been reported at various localities in association with heazlewoodite (Augé et al., 1999) and Ni-rich magnetite (Hudson and Travis, 1981). Some of these Ni-rich awaruite (native Ni) grains might have crystallized from Ni-rich hydrothermal fluids if fS_2 approaches zero and stabilize at sufficiently high fO_2 (Dekov, 2006), or formed by desulfurization (sulfur-loss) of magmatic pentlandite under a strongly reducing conditions (Ramdohr, 1980; Hudson and Travis 1981; Marques de Sá et al., 2018). In contrast, partial dehydration of the La Cabana serpentinites (South-Central Chile) under high-pressure conditions (> 1GPa) generated Ni-rich awaruite in equilibrium with the prograde assemblage antigorite-metamorphic olivine formed within subduction channel at higher fO_2 and fS_2 (González-Jiménez et al., 2021).

At Abu Dahr, native Ni grains (rimming millerite-Fig. 6b) have a composition almost exclusively of Ni (up to 93 wt% Ni) with minor Fe (up to 6.23 wt%) and traces of Cu (up to 1.66 wt% Cu) and Co (up to 0.44 wt% Co). Partial dehydration of the Atg-serpentinites of Abu Dahr South under high-pressure conditions (> 1GPa) generated Ni-rich awaruite in equilibrium with the prograde assemblage antigorite-metamorphic olivine at higher fO_2 and fS_2. These Ni-rich awaruites (native Ni) could register the uptake of Ni from pre-existing Ni-rich sulfides or serpentine, indicating substantial Ni mobility during high P-T metamorphism within subduction channel.

Magnetite is ubiquitous in serpentinites from a variety of environments, ranging from high-temperature magmatic to low-temperature hydrothermal environments (Dare et al., 2014; Nadoll et al., 2014). At Abu Dahr, Ni-rich magnetite (0.40-1.24 wt% NiO) with low Cr content (up to 7.75 wt% Cr_2O_3) reflects its post-magmatic origin. Magnetite formation is commonly described by the reactions R3 and R6. Hydrothermal oxidation of pentlandite (Fig. 5b) to form Ni-rich magnetite has been observed elsewhere (e.g. Ramdohr, 1980; Ballhaus, 1993; Prichard et al., 2013).

Hydrothermal upgrading of Ni-rich sulfide phases. The assemblage pentlandite-heazlewoodite-magnetite formed during the lizarditization stage with atomic sulfur/metal ratio < 1, is indicative of reducing conditions and records very low fO_2 and fS_2 (Frost, 1985; Frost and Beard, 2007; Klein and Bach, 2009; Marchesi et al., 2013; Evans et al., 2017; González-Jiménez et al., 2021). Such low fO_2 is associated with serpentinization at low water/rock ratio (Frost, 1985; Alt and Shanks, 1998). The desulfurization of pentlandite to form heazlewoodite (Figs. 5b and 6a) can be described by the reaction (R12, after Klein and Bach, 2009):

$$Fe_{4.5}Ni_{4.5}S_8 + 6H_2O(aq) = 1.5Ni_3S_2 + 1.5Fe_3O_4 + H_2 + 5H_2S(aq) \quad (12)$$

With increasing fS_2 the assemblage pentlandite-awaruite-magnetite becomes unstable and further reaction of awaruite with H_2S from fluids may result in the formation of heazlewoodite according to reaction R13 (after Klein and Bach, 2009):

$$3Ni_3Fe + 6H_2S(aq) + 4H_2O = 3Ni_3S_2 + Fe_3O_4 + 10H_2(aq) \quad (13)$$

In the presence of extra sulfur (released from desulfurization of pentlandite or released from the subducted slab (Li et al., 2020) as H_2S, Ni remaining after pentlandite upgrade forms new discrete euhedral heazlewoodite grains in partially serpentinized peridotites by the following reaction (R14, after González-Jiménez et al., 2021):

$$3NiO_{(in\ silicate)} + S_{2(aq)} = Ni_3S_2 + 3/2\ O_2 \quad (14)$$

The assemblage pentlandite-heazlewoodite-godlevskite is linked to antigoritization stage accompanied by increasing fO_2 and fS_2. Because low-sulfur godlevskite is found exclusively in fully serpentinized rocks, it is considered that godlevskite replaces heazlewoodite and the formation of godlevskite-rich assemblages (Fig. 5a-d) occur with increasing fO_2 and fS_2 (log fO_2 ~ -32 to ~ -30 (Fig. 11) in the final stage of serpentinization. Formation of godlevskite by direct replacement of heazlewoodite can be described by the reaction R15.

$$3Ni_3S_2 + 2H_2S(aq) = Ni_9S_8 + 2H_2(aq) \quad (15)$$

The assemblage pentlandite-heazlewoodite-godlevskite-millerite is linked to carbonation of the serpentinized peridotites with increasing fO_2 and fS_2. During carbonation of serpentinized peridotites millerite grows at the expense of the low-sulfur heazlewoodite and godlevskite (Fig. 6a). Formation of millerite occurred by direct replacement of low-sulfur sulfides heazlewoodite or godlevskite according to reactions R16 and R17 (after Klein and Bach, 2009):

$$Ni_3S_2 + H_2S(aq) = 3NiS + H_2(aq) \quad (16)$$

$$Ni_9S_8 + H_2S(aq) = 9NiS + H_2(aq) \quad (17)$$

These reactions indicate increasing fO_2 and fS_2 to values above the quartz-fayalite-magnetite (QFM) buffer. According to the phase relations constructed here (Fig. 11), the reactions occur at a range of log fO_2 > ~ -30 and a higher value of log ΣS ~ -1.

The assemblage millerite-native Ni-goethite is linked to partial dehydration of the Atg-serpentinites of Abu Dahr South under high-pressure conditions (> 1GPa). The Ni-rich awaruite is generated in equilibrium with the prograde assemblage antigorite-metamorphic olivine. The increases in $aSiO_2$, fO_2 and fS_2 suggest destabilization of Ni-rich awaruite to more oxidizing assemblages (Sciortino et al., 2015). Under these conditions, millerite is formed by direct replacement of Ni-rich awaruite (Fig. 6b) according to reaction R18:

$$2Ni_3Fe + 6H_2S(aq) + 2O_2 = 6NiS + 2FeOOH + 5H_2(aq) \quad (18)$$

With increasing degree of steatitization (carbonation) magnetite is further oxidized to form goethite (Fig. 6b) indicating higher fO_2. As a result, Fe^{2+} in magnetite is dissolved and precipitated as Fe^{3+} in goethite incorporating Ni (Fe,Ni)O(OH). The overall reactions of magnetite dissolution and goethite formation are represented by R19 and R20 (after He and Traina, 2007):

$$Fe_3O_4 + 2H^+(aq) + 2H_2O = Fe^{2+} + 2Fe(OH)_3 \quad (19)$$

$$2Fe(OH)_3 + 0.5O_2 + 2H^+(aq) = 2FeOOH + 3H_2O \quad (20)$$

Chalcopyrite is absent in all investigated samples from Abu Dahr and occurs only within a steatized sample associated with millerite-rich assemblage (Fig. 6a). The addition of Cu might be explained by hydrothermal fluid infiltration from proximal mafic lithologies (Schwarzenbach et al., 2014). At Abu Dahr, primary chalcopyrite is not present and the rare mineral chalcopyrite

formed by Cu-bearing hydrothermal fluid infiltration from proximal Um Eleiga gabbro complex intruded Abu Dahr Nappe. Cu-dominant Cu-Ni-PGE sulfides (chalcopyrite, bornite, pyrite, pyrrhotite, pentlandite, and mackinawite) do occur in the Um Eleiga gabbro intrusion (Abdel-Halim, 2006).

High Co contents of pentlandite in Abu Dahr

Pentlandite, nominally $(Fe, Ni)_9S_8$, can accommodate variable amounts of Co and Ni in its structure. At Abu Dahr, the cobalt content of pentlandites varies between 1.60 to 7.53 wt%. Based on the reported compositions of Co-pentlandite from different parts of the world (Harris and Nickel, 1972; Brickwood, 1986; Hughes et al., 2016), I classify pentlandite as end-member pentlandite (< 3 wt% Co) or cobaltian pentlandite (>3 up to 20 wt% Co). Cobalt pentlandite (>20 wt% Co) is not detected at Abu Dahr and generally, is a very rare Co-bearing sulfide mineral worldwide. The host peridotites contain magmatic pentlandites, which gradually become enriched in Co during serpentinization. Whole-rock geochemical data show that Ni and Co concentrations range from 1489 to 2590 ppm and 119 to 144 ppm, respectively. There is no significant difference in Ni and Co concentrations between partially and fully serpentinized rocks, suggesting that the serpentinization process occurred isochemically between Ni and Co. Fe, Ni and Co released from primary silicates during serpentinization incorporated into newly formed magnetite and upgrading the Ni-Co tenors of pre-existing primary pentlandite.

The highest concentration of Co in Abu Dahr pentlandites (7.53 wt% Co) is higher than the Co concentrations in pentlandites of komatiitic dunite at Betheno, Western Australia (up to 0.37 wt% Co, Barnes et al., 2011), Dumont pentlandites (average 3.8 wt% Co, Sciortino et al., 2015), and abyssal peridotite pentlandites (up to 4.79 wt% Co, Marchesi et al., 2013). Pentlandites with higher concentrations of Co are reported from Vourinos, Greece (17.7 wt% Co, Tzamos et al.,

2016), Massif du Sud, New Caledonia (13.1 wt% Co, Augé et al. 1999), Cemetery Ridge, Arizona (34.4 wt% Co, Haxel et al., 2018), Santa Elena Nappe, Costa Rica (13.1 wt% Co, Schwarzenbach et al., 2014), and Latao, SE Sulawesi (22.0 wt% Co, Rafianto et al., 2012). High-Co sulfides are also reported from plume magmatism-related mantle peridotite xenoliths (e.g., Wang et al., 2010; Hughes et al., 2016).

Globally, significant Co mineralization is associated with ophiolites (e.g., Bou Azzer, Morocco: Ahmed et al. 2009; and Outokumpu, Finland: Peltonen et al., 2008) or slow-spreading ridges (e.g., Rainbow fields, Mid-Atlantic Ridge; Douville et al., 2002; Mozgova et al. 1996; Borodaev et al. 2007). At Abu Dahr, Co contents in pentlandite are ascribed to sequestration of Ni into heazlewoodite and awaruite, and, furthermore, from the binary plots (Fig. 9a-d), it can be inferred that Co→Fe substitution is dominant in Abu Dahr pentlandites. In addition, strong negative correlations between Co and Fe+Ni and Fe and Co+Ni imply that these elements substituted each other. Similar substitutions were observed in pentlandites from forearc mantle wedge settings worldwide (e.g., Vourinos, Greece: Tzamos et al., 2016; Massif du Sud Peridotite Nappe, New Caledonia: Augé et al. 1999; Cemetery Ridge, Arizona: Haxel et al., 2018; Santa Elena Nappe, Costa Rica: Schwarzenbach et al., 2014; Latao, SE Sulawesi: Rafianto et al., 2012). The cobalt content of pentlandite varies with the degree of serpentinization (Duke 1986), the mineral assemblage with which it is associated (Mozgova et al. 1996), and/or associated with the subduction of Co-enriched oceanic crust (Hughes et al. 2016). One possible explanation for the widespread occurrence of Co-rich pentlandite in Abu Dahr, is that serpentinization took place by reaction of high salinity chloride-rich fluids with cobalt-bearing Ni-Fe alloys, and Co present in the cobalt-bearing Ni-Fe alloys was then released to the fluid and remobilized into the pentlandite (Gagnon et al., 2009)

Similarities to Ni-sulfides and alloys from forearc mantle elsewhere

Table S2 (supplementary material) illustrates the relationships of Ni-sulfides and alloys from Abu Dahr with those reported from mantle wedge serpentinites worldwide (e.g., Vourinos, Greece: Tzamos et al., 2016; Massif du Sud Peridotite Nappe, New Caledonia: Augé et al. 1999; Cemetery Ridge, Arizona: Haxel et al., 2018; Santa Elena Nappe, Costa Rica: Schwarzenbach et al., 2014; Latao, SE Sulawesi: Rafianto et al., 2012; Bou Azzer, Morocco; Ahmed et al., 2009). The minerals show mineralogical and chemical composition similarities (Fig. 12). Some of these occurrences contain beside Ni-sulfides and awaruite Fe-sulfides, arsenides and sulfarsenides (e.g., Bou Azzer, Morocco; Cemetery Ridge, Arizona). Figure 12 shows the distribution of Ni proportions (Ni molar%) of Abu Dahr Ni-sulfide and alloy minerals compared with those reported from Vourinos, New Caledonia, Cemetery Ridge, Santa Elena, Latao, and Bou Azzer. Besides Ni sulfides ± alloys, the Cemetery Ridge peridotites contain two Ni-arsenides and, less commonly, pyrrhotite (Haxel et al., 2018). Santa Elena Nappe contains Cu-pentlandite (Cu < 3 wt%) and chalcopyrite (Schwarzenbach et al., 2014), while the Massif du Sud harzburgites of New Caledonia ophiolite contain Pt-rich Fe-Ni alloy awaruite and native copper (Augé et al. 1999). The Bou Azzer (Morocco) is dominated by Co-Ni arsenide ores, but according to Ahmed et al., (2009) sulfides occur as accessory phases. The chemical, mineralogical and redox conditions reported in this paper suggest that all forearc mantle wedge settings were subjected to similar processes (e.g., Augé et al. 1999; Rafianto et al., 2012; Schwarzenbach et al., 2014, 2021; Tzamos et al., 2016; and Haxel et al., 2018).

Genetic model for Abu Dahr Ni-sulfides and metal alloys

The disseminated Ni mineralization of Abu Dahr consists of high-Ni tenor sulfides and Ni-rich awaruite (native Ni) without Fe sulfides or Ni arsenides. Abu Dahr is one of the

serpentinization-related Ni-Co mineralization worldwide (e.g., Dumont serpentinites (Canada): Sciortino et al., 2015; Bou Azzer serpentinites (Morocco): Ahmed et al., 2009; abyssal serpentinized and talc-altered peridotites: Alt and Shanks 1998, Klein and Bach 2009, Marchesi et al. 2013; Latao (SE Sulawesi): Rafianto et al. 2012; Decar (British Columbia): Britten 2017; Cemetery Ridge (Southwest Arizona): Haxel et al. 2018; Dangoma (Nigeria): Olade, 2019; among others). In all of these occurrences, Ni mineralization is related to hydrothermal alteration accompanying serpentinization of magmatic olivine that liberates Ni-Fe-Co and subsequently forms Ni-rich phases, documenting variations in fO_2 and fS_2. A similar scenario may be suggested in the case of Abu Dahr Ni mineralization, which involved three distinct genetic processes. These are: (1) Desulfurization of magmatic pentlandite and associated sulfur loss that led to formation of heazlewoodite and awaruite during initial serpentinization recording extremely low fO_2 and fS_2 conditions; 2) *In-situ* precipitation of secondary Ni-sulfides in the presence of extra sulfur as aqueous H_2S derived from the desulfurization of magmatic pentlandite or, native Ni when fS_2 approaches 0; and 3) Hydrothermal upgrading of Ni-rich sulfide phases from low-sulfur heazlewoodite to godlevskite in complete serpentinization, and finally to high-sulfur millerite-rich assemblage related to later carbonation recording much higher fO_2.

Implications

The disseminated Ni mineralization in Abu Dahr comprises high nickel concentrates of Ni-rich sulfides and awaruite (native Ni) with neither Fe-sulfides nor Ni-arsenides. Within Abu Dahr forearc environment, high-Ni tenors sulfide and alloy phases such as pentlandite (37 wt% Ni; 7.5 wt% Co), heazlewoodite (71 wt% Ni), godlevskite (67 wt% Ni), millerite (66% Ni wt%) occasionally with awaruite (75-84 wt% Ni) and native Ni (93 wt% Ni) are potentially present. In

this serpentinized environment, pyrite and pyrrhotite are not present. This facilitates production of high grade nickel concentrate after metallurgical process according to IGE Nordic (2010): Ni-rich sulfides + no Fe sulfides + no Ni arsenides constitute a high grade nickel concentrate. The Abu Dahr awaruite contains more Ni content than the compositional range of Dumont awaruite Ni60Fe40-Ni90Fe10 (Sciortino et al., 2015) and those described from the Shetland ophiolite (Prichard et al., 1994) and podiform chromitites (Ahmed and Arai, 2003). Compared with other nickel potential localities worldwide, the Abu Dahr could be a prospective for hydrothermally upgraded Ni-sulfides and Ni-rich awaruite (native Ni). Heat and fluids supplied by the nearby granite intrusions may transport the newly formed sulfides and alloys to suitable trap-sites. Further mineralogical and geochemical studies and geophysical exploration will be required to evaluate the economic potential of the Abu Dahr property.

Acknowledgments

This research was supported, in part, by the project "The Economic Assessment of Platinum in the Eastern Desert of Egypt", Assiut University, Egypt. The insightful comments of Margaux Le Vaillant, B. Ronald Frost, and Mervat A. Elhaddad are highly appreciated. I would like to express my sincere gratitude to Suzanne K. Birner and Xiaolu Niu for providing me with Excel spreadsheet programs for P-T and oxygen fugacity calculations. I would like to thank the editorial board; Hongwu Xu, American Mineralogist Editor and Kate Kiseeva, Associate Editor are thanked for their help through research submission and their valuable comments and suggestions on my manuscript. The reviewers Katy A. Evans and Michael Zelenski are thanked for constructive reviews and their insightful comments and suggestions that improved the manuscript.

References Cited

Abdel-Halim, A.H. (2006) Mineralogy and geochemistry of the mafic-ultramafic rocks and associated mineralization at Abu Dahr and El Motaghairat, Eastern Desert, Egypt. Unpublished Ph.D. thesis, Minia University, Egypt.

Abdel-Halim, A.H., Helmy, H.M., ElHaddad, M.A., El Mahallawi, M.M., and Mogessie, A. (2020) Petrology of a Neoproterozoic mantle peridotite-chromitite association from Abu Dahr area Eastern Desert Egypt, Infiltration of a boninitic melt in highly depleted harzburgite. Journal African Earth Sciences, 165, 103816.

Abdel-Karim A.M., Azer M. K., Mogahed M.M. 2021, Neoproterozoic concentric intrusive complex of gabbro-diorite-tonalite-granodiorite association, Rahaba area, southern Eastern Desert of Egypt: Implications for magma mixing of arc intrusive rocks. Lithos 404–405, 106423.

Abdel-Khalek M.L., Takla, M.A., Sehim, A., Hamimi, Z., and El Manawi, A.W. (1992) Geology and tectonic evolution of Wadi Beitan area, Southeastern Desert, Egypt. Geology of Arab World, 1, 369-394.

Abrajano, T. A. and Pasteris, J. D. (1989) Zambales ophiolite, Philippines, II. Sulfide petrology of the critical zone of the Acoje Massif. Contributions to Mineralogy and Petrology 103, 64-77

Ahmed, A.H., Arai, S., and Ikenne, M. (2009) Mineralogy and paragenesis of the Co-Ni arsenide ores of Bou Azzer Anti-Atlas Morocco. Economic Geology, 104, 249-266.

Albers, E., Kahl, W., Beyer, L., and Bach, W. (2020) Variant across-forearc compositions of slab-fluids recorded by serpentinites: Implications on the mobilization of FMEs from an active subduction zone (Mariana forearc). Lihos, 364-365, 105525.

Alt, J. C., and Shanks, W. C. (1998) Sulfur in serpentinized oceanic peridotites: Serpentinization processes and microbial sulphate reduction. Journal of Geophysical Research, 103, 9917-9929.

Alt, J. C., Shanks, W. C., Bach, W., Paulick, H., Garrido, C. J., and Beaudoin, G. (2007) Hydrothermal alteration and microbial sulphate reduction in peridotite and gabbro exposed by detachment faulting at the Mid-Atlantic Ridge, 15° 20' N (ODP Leg 209): A sulfur and oxygen isotope study. Geochemistry, Geophysics, Geosystems, 8.

Arai, S. (1992) Chemistry of chromian spinel in volcanic rocks a potential guide to magma chemistry. Mineralogical Magazine, 56, 173-184.

Arai, S. (1994) Characterization of spinel peridotites by olivine-spinel compositional relationships, review and interpretation. Chemical Geology, 113, 191-204.

Arai, S., and Ishimaru, S. (2007) Insights into petrological characteristics of the lithosphere of mantle wedge beneath arcs through peridotite xenoliths: A review. Journal of Petrology, 49, 665-695.

Ashmawy, M.H. (1987) The ophiolitic mélange of the South Eastern Desert of Egypt: Remote sensing, field work and petrographic investigations. Dissertation Berliner Geowiss Abh Berlin.

Auclair, M., Gauthier, M., Trottier, J., Jebrak, M., and Chartrand, F. (1993) Mineralogy geochemistry and paragenesis of the Eastern Metals serpentinite-associated Ni-Cu-Zn deposit Quebec Appalachians. Economic Geology, 88, 123-138.

Augé, T.Y., Cabri, L.J., Legendre, O., McMahon, G., and Cocherie, A. (1999) PGE distribution in base-metal alloys and sulfides of the New Caledonia Ophiolite. Canadian Mineralogist, 37, 1147-1161.

Azer, M.K., and Stern, R.J. (2007) Neoproterozoic (835-720 Ma) serpentinites in the Eastern Desert, Egypt, Fragments of forearc mantle. The Journal of Geology, 115, 457-472.

Azer, M.K., Asimow, P.D., 2021. Petrogenetic Evolution of the Neoproterozoic Igneous Rocks of Egypt. In The Geology of the Egyptian Nubian Shield. Springer, pp. 343–382.

Bach, W., Paulick, H., Garrido, C.J., Ildefonse, B., Meurer, W.P., and Humphris, S.E. (2006) Unraveling the sequence of serpentinization reactions, petrography mineral chemistry and petrophysics of serpentinites from MAR 15°N (ODP Leg 209 Site 1274). Geophysical Research Letters 33 doi,101029/2006GL025681.

Ballhaus, C. (1993) Oxidation states of the lithospheric and asthenospheric upper mantle. Contributions to Mineralogy and Petrology, 114, 331-348.

Ballhaus, C., Berry, R.F., and Green, D.H. (1991) High pressure experimental calibration of the olivine-orthopyroxene-spinel oxygen geobarometer: Implications for the oxidation state of the upper mantle. Contributions to Mineralogy and Petrology, 107, 27-40.

Barnes, S.J., Wells, M.A., and Verrall, M.R. (2009) Effects of magmatic processes, serpentinization and talc-carbonate alteration on sulfide mineralogy and ore textures in the Black Swan disseminated nickel sulfide deposit, Yilgarn Craton. Economic Geology, 104, 539-562.

Barnes, S.J., Godel, B.M., Locmelis, M., Fiorentini, M.L., and Ryan, C.G. (2011) Extremely Ni-rich Fe-Ni sulfide assemblages in komatiitic dunite at Betheno, Western Australia: Results from synchrotron X-ray fluorescence mapping. Australian Journal of Earth Sciences, 58, 691-709.

Barnes, S.J., Godel, B., Gürer, D., Brenan, J.M., Roberston, J., and Paterson, D. (2013) Sulfide-olivine Fe-Ni exchange and the origin of anomalously Ni-rich magmatic sulfides. Economic Geology, 108, 1971-1982.

Bénard, A., Woodland, A. B., Arculus, R. J., Nebel, O., and McAlpine, S. R. (2018). Variation in sub-arc mantle oxygen fugacity during partial melting recorded in refractory peridotite xenoliths from the West Bismarck Arc. Chemical Geology, 486, 16-30.

Birner, S.K., Warren, J.W., Cottrell, E., Davis, F.A. (2016) Hydrothermal alteration of seafloor peridotites does not influence oxygen fugacity recorded by spinel oxybarometry. Geology 44, 7, 535–538.

Birner, S.K., Warren, J.W., Cottrell, E., Davis, F.A., Kelley, K.A., and Falloon, T.J. (2017) Forearc peridotites from Tonga record heterogeneous oxidation of the mantle following subduction initiation. Journal of Petrology, 58, 1755-1780.

Borodaev, Yu.S., Bryzgalov, I.A., Mozgova, N.N., and Uspenskaya, T.Yu. (2007) Pentlandite and Co-enriched pentlandite as characteristic minerals of modern hydrothermal sulfide mounds hosted by serpentinized ultramafic rocks (Mid-Atlantic Ridge). Moscow Univ. Geological Bulletin, 62 (2), 85-97.

Boskabadi, A., Pitcairn, I.K., Leybourne, M.I., Teagle, D.A., Cooper, M.J., Hadizadeh, H., et al. (2020) Carbonation of ophiolitic ultramafic rocks: Listvenite formation in the Late Cretaceous ophiolites of eastern Iran. Lithos, 352, 105307.

Brey, G.P., and Köhler, T., (1990) Geothermobarometry in four-phase lherzolites II. New thermobarometers, and practical assessment of existing thermobarometers: Journal of Petrology, 31, 1353-1378.

Brickwood, J.D. (1986) The geology and mineralogy of some Fe-Cu-Ni sulphide deposits in the Bamble area, Norway. Norsk Geologisk Tidsskrift, 66, 189-208.

Britten, R. (2017) Regional metallogeny and genesis of a new deposit type-disseminated awaruite (Ni_3Fe) mineralization hosted in the Cache Creek Terrane. Economic Geology, 112(3), 517-550.

Ciazela, J., Dick, H., Koepke, J., Botcharnikov, R., Muszynski, A., and Kuhn, T. (2015) Cu refertilization of abyssal harzburgites by melt percolation. Geophysical Research Abstracts, 17, EGU2015-1044.

Clarke, E., De Hoog, J.C.M., Kirstein, L.A., Harvey, J., Debret, B. (2020) Metamorphic olivine records external fluid infiltration during serpentinite dehydration. Geochemical Perspective Letter 16, 25-29.

Dare, S.A.S., Pearce, J.A., McDonald, I., and Styles, M.T. (2009) Tectonic discrimination of peridotites using fO2-Cr# and Ga-Ti-FeIII systematic in chrome-spinel: Chemical Geology 261, 199-216.

de Obeso, J.C., Kelemen, P.B. (2020) Major element mobility during serpentinization, oxidation and weathering of mantle peridotite at low temperatures. Philosophical Transactions Royal Society A, 378, 20180433.

Debret B., Nicollet, C., Andreani, M., Schwartz, S., and Godaed, M. (2013) Three steps of serpentinization in an eclogitized oceanic serpentinization front (Lanzo Massif-Western Alps): Journal metamorphic Geology, 31, 165-186.

Debret, B., Albers, E., Walter, B., Price, R., Barnes, J.D., Beunon, H., Facq, S., Gillikin, D.P., Mattielli, N., and Williams, H. (2019) Shallow forearc mantle dynamics and geochemistry: New insights from IODP Expedition 366. Lithos, 326-327, 230-245.

Debret, B., Reekie, C.D.J., Mattielli, N., Beunon, H., Ménez, B., Savov, I.P., and Williams, H.M. (2020) Redox transfer at subduction zones: insights from Fe isotopes in the Mariana forearc. Geochemical Perspectives Letters, 12, 46-51.

Dekov, V. (2006) Native nickel in the TAG hydrothermal sediments (Mid-Atlantic Ridge 26p N), space trotter guest from the mantle or widespread mineral connected with serpentinization? Journal Geophysical Research, 111, B5.

Delacour, A., Fruh-Green, G. L., Bernasconi, S. M., and Kelley, D. S. (2008) Sulfur in peridotites and gabbros at Lost City (30°N, MAR): Implications for hydrothermal alteration and microbial activity during serpentinization. Geochimica et Cosmochimica Acta, 72, 5090-5110.

Deschamps, F., Guillot, S., Godard, M., Chauvel, C., Andreani, M., Hattori, K., 2010. In situ characterization of serpentinites from forearc mantle wedges: timing of serpentinization and behavior of fluid-mobile elements in subduction zones. Chem. Geol. 269, 262–277. https://doi.org/10.1016/j.chemgeo.2009.10.002.

Deschamps, F., Godard, M., Guillot, S., and Hattori, K. (2013) Geochemistry of subduction zone serpentinites: a review. Lithos, 178, 96-127.

Dick, H.J.B., and Bullen, T. (1984) Chromian spinel as a petrogenetic indicator in abyssal and alpine-type peridotites and spatially associated lavas. Contributions to Mineralogy and Petrololgy, 86, 54-76.

Donaldson, M.J. (1981) Redistribution of ore elements during serpentinization and talc-carbonate alteration of some Archean dunites Western Australia. Economic Geology, 76, 1698-1713.

Douville, E., Charlou, J.L., Oelkers, E.H., Bienvenu, P., Jove Colon, C.F., Donval, J.P., Fouquet, Y., Prieur, D., and Approu, P. (2002) The rainbow vent fluids (36°14′N, MAR): the influence of ultramafic rocks and phase separation on tracemetal content in Mid-Atlantic Ridge hydrothermal fluids. Chemical Geology, 184, 37-48.

Duke, J.M. (1986) Petrology and economic geology of the Dumont Sill: An archean intrusion of komatiitic affinity in northwestern Quebec. Geological Survey of Canada, Economic Geology Report, 35, 1-56.

Eckstrand, O.R. (1975) The Dumont serpentinite, A model for control of nickeliferous opaque mineral assemblages by alteration reactions in ultramafic rocks. Economic Geology, 70, 183-201.

El Tahlawi, M.R., Khudeir, A.A., and Bishara, W. (1997) An inquiry into the tectonic setting of an ophiolite association from Egypt. Third Conference of Geochemistry, Alexandria, Egypt, 1, 395-408.

Evans K. A. (2006) Redox decoupling and redox budgets: conceptual tools for the study of earth systems. Geology, 34, 489.

Evans, K.A. (2012) The redox budget of subduction zones. Earth-Science Reviews, 113(1-2), 11-32.

Evans, K.A., and Frost, B.R. (2021) Deserpentinization in subduction zones as a source of oxidation in arcs: a reality check. Journal of Petrology, 1-32.

Evans, K.A., and Tomkins, A.G. (2011) The relationship between subduction zone redox budget and arc magma fertility: Earth and Planetary Science Letters, 308, 401-409.

Evans, K.A., Elburg, M A., and Kamenetsky, V.S. (2012) Oxidation state of subarc mantle. Geology, 40(9), 783-786.

Evans, K.A., Reddy, S.M., Tomkins, A.G., Crossley, R.J., and Frost, B.R. (2017) Effects of geodynamic setting on the redox state of fluids released by subducted mantle lithosphere. Lithos, 278, 26-42.

Filippidis, A. (1985) Formation of awaruite in the system Ni-Fe-Mg-Si-O-H-S and olivine hydration with NaOH solution, an experimental study. Economic Geology, 80, 1974-1980.

Foustoukos, D.I., Bizimis, M., Frisby, C., and Shirey, S.B. (2015) Redox controls on Ni-Fe-PGE mineralization and Re/Os fractionation during serpentinization of abyssal peridotite. Geochimica et Cosmochimica Acta, 150, 11-25.

Frost, B., Evans, K.A., Swapp, S.M., Beard, J.S., and Mothersole, F.E. (2013) The process of serpentinization in dunite from New Caledonia. Lithos, 178, 24-39.

Frost, B.R., and Beard, J.S. (2007) On silica activity and serpentinization. Journal of Petrology, 48, 1351-1368.

Frost, D.J. and McCammon, C.A. (2008) The Redox State of Earth's Mantle. Annual Review Earth Planetary Science 36:389-420.

Frost, R.B. (1985) On the stability of sulfides oxides and native metals in serpentinite. Journal of Petrology, 26, 31-63.

Gahlan, H.A., Azer, M.K., and Khalil, A. (2015) The Neoproterozoic AD ophiolite South Eastern Desert Egypt Petrological characteristics and tectonomagmatic evolution. Mineralogy and Petrology, 109, 611-630.

González-Álvarez, I., Pirajno, F., and Kerrich, R. (2013) Hydrothermal nickel deposits secular variation and diversity. Ore Geology Reviews, 52, 1-3.

González-Jiménez, J.M., Piña, R., Saunders, J.E., Plissart, G., Marchesi, C., et al. (2021) Trace element fingerprints of Ni-Fe-S-As minerals in subduction channel serpentinites. Lithos, 400, 106432.

Groves, D.I., Hudson, D.R., and Hack, T.B.C. (1974) Modification of iron-nickel sulfides during serpentinization and talc-carbonate alteration at Black Swan, Western Australia. Economic Geology, 69, 1265-1281.

Guillot, S., Hattori, K.H., and de Sigoyer, J. (2000) Mantle wedge serpentinization and exhumation of eclogites, Insights from eastern Ladakh northwest Himalaya. Geology, 28, 199-202.

Harris, D.C., and Nickel, E.H. (1972) Pentlandite compositions and associations in some mineral deposits. Canadian Mineralogist, 11, 861-878.

Harvey J., Warren J. M. and Shirey S. B. (2016) Mantle sulfides and their role in Re-Os and Pb isotope geochronology. Reviews in Mineralogy and Geochemistry, 81, 579-649.

Hattori, K.H., and Guillot, S. (2007) Geochemical character of serpentinites associated with high- to ultrahigh-pressure metamorphic rocks in the Alps Cuba and the Himalayas, Recycling of elements in subduction zones. Geochemistry Geophysics Geosystem 8.

Haxel, G.B., Wittke, J.H., Epstein, G.S., and Jacobson, C.E. (2018) Serpentinization-related nickel, iron, and cobalt sulfide, arsenide, and intermetallic minerals in an unusual inland tectonic setting, southern Arizona, USA. in Ingersoll, R.V., Graham, S.A. and Lawton, T.F. eds, Tectonics Sedimentary Basins and Provenance, A Celebration of William R Dickinson's Career. Geological Society of America, Special Paper, 540, 65-87.

He, Y.T. and Traina, S.J. (2007) Transformation of magnetite to goethite under alkaline pH conditions. Clay Minerals, 42, 13-19.

Hellebrand. E., Snow, J.E., Dick, H.J.B., and Hofmann, A.W. (2001) Coupled major and trace elements as indicator of the extent of melting in mid-ocean-ridge peridotites. Nature, 410, 677-681.

Herzberg, C., Vidito, C., and Starkey, N.A. (2016) Nickel-cobalt contents of olivine record origin of mantle peridotite and related rocks. American Mineralogist, 101, 1952-1966.

Hoatson, D., and Sun, A.S. (2002) Archean layered mafic-ultramafic intrusions in the West Pilbara Craton Western Australia a synthesis of some of the oldest orthomagmatic mineralizing systems in the world. Economic Geology, 97, 847-872.

Hudson, D.R., and Travis, G.A. (1981) A native nickel-heazlewoodite-ferroan trevorite assemblage from Mount Clifford Western Australia. Economic Geology, 76, 1686-1697.

Hughes, H.S.R., McDonald, I., Faithfull, J.W., Upton, B.G.J., and Loocke, M. (2016) Cobalt and precious metals in sulfides of peridotite xenoliths and inferences concerning their distribution according to geodynamic environment A case study from the Scottish lithospheric mantle. Lithos, 240-243, 202-227.

Hyndman, R.D., and Peacock, S.M. (2003) Serpentinization of the forearc mantle. Earth and Planetary Science Letters, 212, 417-432.

IGE Nordic (2010) Ronnbacken-Developing a major nickel sulfide project in Sweden. Raw Materials Group 7th Annual Exploration and Mining Investment Conference, Stockholm.

Ishii, T., Robinson, P.T., Maekawa, H., and Fiske, R. (1992) Petrological studies of peridotites from diapiric serpentinite seamounts in the Izu-Ogasawara-Mariana forearc, Leg 125. In, Fryer, P., Pearce, J.A., Stokking, L.B., et al. (Eds.), Proceedings of the Ocean Drilling Program Scientific Results, 125, 445-486.

Ishimaru, S., Arai, S., and Shukuno, H. (2009) Metal-saturated peridotite in the mantle wedge inferred from metal-bearing peridotite xenoliths from Avacha volcano, Kamchatka. Earth and Planetary Science Letters, 284(3-4).

Kamenetsky, V.S., Lygin, A.V., Foster, J.G., Meffre, S., Maas, R., Kamenetsky, M.B., Goemann, K., and Beresford, S.W. (2016) A story of olivine in the McIvory Hill complex Tasmania Australia, clues to the origin of Avebury metasomatic Ni sulfide deposit. American Mineralogist, 101, 1321-1331.

Kaneda, H., Takenouchi, S., and Shoji, T. (1986) Stability of pentlandite in the Fe-Ni-Co-S system. Mineralium Deposita, 21, 169-180.

Keays, R.R., and Jowitt, S.M. (2013) The Avebury Ni deposit Tasmania a case study of an unconventional nickel deposit. Ore Geology Reviews, 52, 4-17.

Kelley, K.A. and Cottrell, E. (2009) Water and the oxidation state of subduction zone magmas. Science, 325, 605-607.

Khedr, M.Z., and Arai, S. (2013) Origin of Neoproterozoic ophiolitic peridotites in South Eastern Desert Egypt constrained from primary mantle mineral chemistry. Mineralogy and Petrology, 107, 807-828.

Khedr, M.Z., and Arai, S. (2016) Chemical variations of mineral inclusions in Neoproterozoic high-Cr chromitites from Egypt Evidence of fluids during chromitite genesis. Lithos, 240-243, 309-326.

Khedr, M.Z., Takazawa, E., Hauzenberger, C., Tamura, A., Arai, S., Stern, R.J., Morishita, T., and El-Awady, A. (2022) Petrogenesis of arc-related serpentinized peridotites (Egypt): insights into Neoproterozoic mantle evolution beneath the Arabian-Nubian Shield. Journal of Asian Earth Sciences, 105078.

Kilgore, M.L., Peslier, A.H., Brandon, A.D., and Lamb, W.M. (2018) Water and oxygen fugacity in the lithospheric mantle wedge beneath the northern Canadian Cordillera (Alligator Lake). Geochemistry, Geophysics, Geosystems, 19.

Kiseeva, E.S., Fonseca, R.O.C., and Smythe, D.J. (2017) Chalcophile elements and sulfides in the upper mantle. Elements, 13, 111-116.

Klein, F., and Bach, W. (2009) Fe-Ni-Co-O-S Phase relations in peridotite-seawater interactions. Journal of Petrology, 501, 37-59.

Le Vaillant, M., Saleem, A., Barnes, S.J., Fiorentini, M.L., Miller, J., Beresford, S., and Perring, C. (2016) Hydrothermal remobilisation around a deformed and remobilised komatiite-hosted Ni-Cu-(PGE) deposit, Sarah's Find, Agnew Wiluna greenstone belt, Yilgarn Craton, Western Australia. Mineralium Deposita, 51, 369-388.

Li, J-L., Schwarzenbach, E.M., John, T. et al (2020) Uncovering and quantifying the subduction zone sulfur cycle from the slab perspective. Nature Communications, 11,514.

Lian, D., Yang, J., Dilek, Y., and Rocholl, A. (2018) Mineralogy and geochemistry of peridotites and chromitites in the Aladag ophiolite (southern Turkey), melt evolution of the Cretaceous Neotethyan mantle. Journal of Geological Society, https,//doiorg/101144/jgs2018-060.

Lorand, J. P. (1989) Mineralogy and chemistry of Cu-Fe-Ni sulfides in orogenic-type spinel peridotite bodies from Ariege (northeastern Pyrenees, France). Contributions to Mineralogy and Petrology 103, 335-345.

Lorand, J.P., and Luguet, A. (2016) Chalcophile and siderophile elements in mantle rocks, trace elements controlled by trace minerals. Reviews in Mineralogy and Geochemistry, 81, 441-488.

Malaspina, N., Poli, S., and Fumagalli, P. (2009) The Oxidation State of Metasomatized Mantle Wedge: Insights from C-O-H-bearing Garnet Peridotite. Journal of Petrology, 50, 1533-1552.

Malaspina, N., Langenhorst, F., Tumiati, S., Campione, M., Frezzotti, M.L. and Poli, S. (2017) The redox budget of crust-derived fluid phases at the slab- mantle interface. Geochimica et Cosmochimica Acta, 209.

Marchesi, C., Garrido, C.J., Harvey, J., González-Jiménez, J-M., Hidas, K., Lorand, J-P., and Gervilla, F. (2013) Platinum-group elements S Se and Cu in highly depleted abyssal peridotites from the Mid-Atlantic Ocean Ridge (ODP Hole 1274A): Influence of hydrothermal and magmatic processes. Contributions to Mineralogy and Petrology, 166, 1521-1538.

Marques de Sá, C.D., Martins, B.L.L., Barreto, D.S., Paim, M., and Conceicao, H. (2018) First finding of native Nickel in cumulates of the Canindé Domain Brazil. Divulgação Científica E Tecnológica DO IFPB No 43.

Marques, A.F.A., Barriga, F.J.A.S., and Scott, S.D. (2007) Sulfide mineralization in an ultramafic-rock hosted seafloor hydrothermal system from serpentinization to the formation of Cu-Zn-(Co)-rich massive sulfides. Marine Geology, 245, 20-39.

Miller, D. J. (2007) Sulfide mineralization at Site 1268, Mid-Atlantic Ridge, Ocean Drilling Program Leg 209. In: Kelemen, P. B., Kikawa, E. and Miller, D. J. (eds.) Proceedings of the Ocean Drilling Program; Scientific Results, 209. College Station, TX: Ocean Drilling Program, 18 pp.

Misra, K.C., and Fleet, M.E. (1973) The Chemical compositions of synthetic and natural pentlandite assemblages. Economic Geology, 68, 51-530.

Mozgova, N.N., Krasnov, S.G., Batuyev, B.N., Borodaev, Y.S., Efimov, A.V., Markov, V.F., and Stepanova, T.V. (1996) The first report of cobalt pentlandite from a Mid-Atlantic Ridge hydrothermal deposit. Canadian Mineralogist, 34, 23-28.

Murata, K., Maekawa, H., Yokose, H., Yamamoto, K., Fujioka, K., Ishii, T., Chiba, H., and Wada, Y. (2009) Significance of serpentinization of wedge mantle peridotites beneath Mariana forearc western Pacific: Geosphere, 5, 90-104.

Nadoll, P., Angerer, T., Mauk, J.L., French, D., and Walshe, J. (2014) The Chemistry of hydrothermal magnetite, A review. Ore Geology Reviews, 61, 1-32.

Negishi, H., Arai, S., Yurimoto, H., Ito, S., Ishimaru, S., Tamura, A., and Akizawa, N. (2013) Sulfide-rich dunite within a thick Moho transition zone of the northern Oman ophiolite, Implications for the origin of Cyprus-type sulfide deposits. Lithos, 164-167, 22-35.

Nikkola, P., Guðfinnsson, G.H., Bali, E. et al. (2019) Signature of deep mantle melting in South Iceland olivine. Contributions to Mineralogy and Petrology 174, 1-19.

Olade, M.A. (2019) Perspectives on the recently-discovered native nickel deposit in Dangoma Kaduna State Nigeria. Achievers Univ. Journal of Scientific Research, 2 (1).

Padron-Navarta, J.A., Sanchez-Vizcaino, V.L., Garrido, C.J., and Gomez-Pugnaire, M.T. (2011) Metamorphic record of high-pressure dehydration of antigorite serpentinite to chlorite harzburgite in a subduction setting (Cerro del Almirez, Nevado-Filábride Complex, southern Spain). Journal of Petrology, 52, 2047-2078.

Palme, H., and O'Neill, H.St.C. (2003) Cosmochemical estimates of mantle composition in Carlson RW ed The mantle and core. Treatise on Geochemistry, 2, 1-28.

Parkinson, J. and Arculus, R.J. (1999) Redox state of subduction zones: insights from arc-peridotites. Chemical Geology, 160, 408-423.

Parkinson, J. and Pearce, J.A. (1998) Peridotites of the Izu-Bonin-Mariana forearc (ODP Leg 125) evidence for mantle melting and melt-mantle interactions in a supra-subduction zone setting. Journal of Petrology, 39, 1577-1618.

Pearce, J.A., Barker, P.F., Edwards, S.J., Parkinson, I.J., and Leat, P.T. (2000) Geochemistry and tectonic significance of peridotites from the South Sandwich arc-basin system South Atlantic. Contributions to Mineralogy and Petrology, 139, 36-53.

Peltonen, P., Kontinen, A., Huhma, H., and Kuronen, U. (2008) Outokumpu revisited, new mineral deposit model for the mantle peridotite-associated Cu-Co-Zn-Ni-Ag-Au sulphide deposits. Ore Geology Reviews, 33, 559-617.

Perinelli, C., Andreozzi, G.B., Conte, A.M., Oberti, R., and Armient, P. (2012) Redox state of subcontinental lithospheric mantle and relationships with metasomatism: insights from spinel peridotites from northern Victoria Land (Antarctica). Contributions to Mineralogy and Petrology, 164, 1053-1067.

Pirajno, F. (2009) Hydrothermal Processes and Mineral Systems. Geological Survey of Western Australia Springer, 1250 p.

Pirajno, .F, and González-Álvarez, I. (2013) A re-assessment of the Epoch Ni deposit Filabusi greenstone belt Zimbabwe a possible hydrothermal system. Ore Geology Reviews, 52, 58-65.

Prichard, H.M., Lxer, R., Lord, R.A., Maynard, J., and Williams, N. (1994) Assemblages of platinum-group minerals and sulfides in silicate lithologies and chromite-rich rocks within the Shetland ophiolite. Canadian Mineralogist, 32, 271-294.

Prichard, H.M., Knight, R.D., Fisher, P.C., McDonald, I., Zhou, M-F., and Wang, C.Y. (2013) Distribution of platinum-group elements in magmatic and altered ores in the Jinchuan intrusion China an example of selenium remobilization by post magmatic fluids. Minalium Deposita, 48, 767-786.

Putirka, K.D. (2008) Thermometers and Barometers for volcanic systems. Review Mineralogy Geochemistry 69, 61-120.

Rafianto, R., Attong, F., Matano, A., and Noor, M.E.S. (2012) The serpentine-related nickel sulphide occurrences from Latao SE Sulawesi; a new frontier of nickel exploration in Indonesia. Majalah Geologi Indonesia, 27 (2), 87-107.

Ramdohr, P. (1980) The Ore Minerals and their Intergrowths. Pergamon Press, Oxford, England.

Rielli, A., Tomkins, A.G., Nebel, O., Brugger, J., Etschmann, B., Zhong, R., Yaxley, G.M., and Paterson, D. (2017) Evidence of sub-arc mantle oxidation by sulphur and carbon. Geochemical Perspectives Letters, 3 (2), 124-132.

Rottier, B., Kouzmanov, K., Wälle, M., Bendezú, R., and Fontboté, L. (2016) Sulfide replacement processes revealed by textural and LA–ICP–MS trace element analyses: Example from the early mineralization stages at Cerro de Pasco, Peru. Economic Geology 111: 1347–1367.

Schwartz, S., Guillot, S., Reynard, B., Lafay, R., Debret, B., Nicollet, C., Lanari, P., and Auzende, A.L. (2013) Pressure-temperature estimates of the lizardite/antigorite transition in high pressure serpentinites. Lithos, 178, 197-210.

Scambelluri, M., Müntener, O., Ottolini, l., Pettke, T.T., Vannucci, R. (2004) The fate of B, Cl and Li in the subducted oceanic mantle and in the antigorite breakdown fluids. Earth and Planetary Science Letters 222, 217-234.

Schwarzenbach, E.M., Gazel, E., and Caddick, M. J. (2014) Hydrothermal processes in partially serpentinized peridotites from Costa Rica: Evidence from native copper and complex sulfide assemblages. Contributions to Mineralogy and Petrology, 168, 1-21.

Schwarzenbach, E. M., Vrijmoed, J. C., Engelmann, J. M., Liesegang, M., Wiechert, U., Rohne, R., and Plümper, O. (2021). Sulfide dissolution and awaruite formation in continental

serpentinization environments and its implications to supporting life. Journal of Geophysical Research: Solid Earth, 126.

Sciortino, M., Mungall, J.E., and Muinonen, J. (2015) Generation of high-Ni sulfide and alloy phases during serpentinization of dunite in the Dumont Sill Quebec. Economic Geology, 110, 733-761.

Secchiari, A., Montanini, A., Bosch, D., and Macera, P. (2020) Sr Nd Pb and trace element systematics of the New Caledonia harzburgites, Tracking source depletion and contamination processes in a SSZ setting. Geoscience Frontiers, 11, 37-55.

Shackleton, R.M. (1994) Review of Late Proterozoic sutures ophiolitic mélanges and tectonics of eastern Egypt and nort-east Sudan. Geologic Rundsch, 83, 537-546.

Shiga, Y. (1987) Behavior of iron nickel cobalt and sulfur during serpentinization with reference to the Hayachine Ultramafic Rocks of the Kamaishi mining district Northeastern Japan. Canadian Mineralogist, 25, 611-624.

Simon, N.S.C., Neumann, E., Bonadiman, O., et al. (2008) Ultra-refractory domains in the oceanic mantle lithosphere sampled as mantle xenoliths at ocean islands. J. Petrol. 49, 1223–1251.

Sobolev, A.V., Hofmann, A.W, Sobolev, S.V., and Nikogosian, I.K. (2005) An olivine-free mantle source of Hawaiian shield basalts. Nature 434:590-597. https://doi.org/10.1038/nature03411 Sobolev, A.V., Hofmann, A.W., Kuzmin, D.V. et al (2007) The amount of recycled crust in sources of mantle-derived melts. Science, 316:412-417.

Stern, R.J., Johnson, P.R., Kröner, A., and Yibas, B. (2004) Neoproterozoic ophiolites of the Arabian-Nubian Shield in Kusky TM ed Precambrian ophiolites and related rocks. Elsevier Amsterdam, 95-128.

Tzamos, E., Filippidis, A., Michailidis, K., Koroneos, A., Rassios, A., Grieco, G., Pedrotti, M., and Stamoulis, K. (2016) Mineral chemistry and formation of awaruite and heazlewoodite in the Xerolivado Chrome mine Vourinos Greece. Bulletin of the Geological Society of Greece L, 2047-2056.

Ulmer, P. and Trommsdorff, V. (1995) Serpentine stability to mantle depths and subduction-related magmatism: Science, 268, 858-861.

Vaughan, D.J., and Corkhill, C. (2017) Mineralogy of sulfides. Elements, 13, 83-89.

Wang, J., Xiong, X., Chen, Y., and Huang, F. (2020) Redox processes in subduction zones. Progress and prospect. Science China Earth Sciences, 63.

Wang, K-L., O'Reilly, S.Y., Honda, M., Matsumoto, T., Griffin, W.L., Pearson, N.J., and Zhang, M. (2010) Co-rich sulfides in mantle peridotites from Penghu Islands Taiwan footprints of Proterozoic mantle plumes under the Cathaysia Block. Journal of Asian Earth Sciences, 37, 229-245.

Wang, X., Zeng, Z., and Chen, J. (2009) Serpentinization of peridotites from the southern Mariana forearc. Progress in Natural Science, 19, 1287-1295.

Wells, P.R.A. (1977) Pyroxene thermometry in simple and complex systems: Contributions to Mineralogy and Petrology, 62, 129–139.

Whitney, D.L. and Evans, B.W. (2010) Abbreviations for names of rock-forming minerals. American Mineralogist, 95, 185-187.

Wood, B.J. and Banno, S. (1973) Garnet-orthopyroxene and orthopyroxene-clinopyroxene relationships in simple and complex systems: Contributions to Mineralogy and Petrology 42, 109-124.

Wu, W., Yang, J., Dilek, Y., Milushi, I. and Lian, D. (2017) Multiple episodes of melting, depletion, and enrichment of the Tethyan mantle: petrogenesis of the peridotites and chromitites in the Jurassic Skenderbeu massif, Mirdita ophiolite, Albania. Lithosphere, 10, 54–78.

Zheng, Y.F., Xu, Z., Chen, L., Dai, L.Q., and Zhao, Z.F. (2020) Chemical geodynamics of mafic magmatism above subduction zones. Journal of Asian Earth Sciences, 194, 104185.

Zoheir, B.A., Mehanna, A.M., and Qaoud, N.N. (2008) Geochemistry and geothermobarometry of the Um Eleiga Neoproterozoic island-arc intrusive complex SE Egypt genesis of a potential gold-hosting intrusion. Applied Earth Sciences, 117, 89-111.

Table captions

Table 1. GPS coordinates of the observation points (OP) sampled from Abu Dahr peridotites.

Table 2. Primary and secondary Ni-bearing phases in serpentinized peridotites of Abu Dahr with referring to mineral abbreviation used in this study.

Table 3. Representative EMP analyses of pentlandite Pn and cobaltian pentlandite Co Pn in Abu Dahr serpentinized peridotites.

Table 4. Representative EMP analyses of heazlewoodite Hzl, godlevskite Gv, millerite Mlr, chalcopyrite Ccp, awaruite Awr, and native Ni in Abu Dahr serpentinized-carbonated peridotites.

Table 5. Representative EMP analyses and Ni contents (ppm) of ferritchromite Fe-Chr, magnetite Mag and goethite Gth from Abu Dahr serpentinized peridotites. ppm Ni = wt% NiO*10000/1.273

Table 6. Calculated equilibrium P-T and oxygen fugacities for Abu Dahr harzburgites

Table 7. Whole-rock major oxides (wt%) normalized on a volatile-free basis and trace elements (ppm) contents of Abu Dahr serpentinized harzburgites.

Table S1. Representative EMP analyses (wt%) and Ni contents (ppm) of olivines, spinels, ortho- and clinopyroxenes and Ca-amphiboles from Abu Dahr harzburgites.

Table S2. Correlation of Abu Dahr Ni sulfides and alloys (element compositions) with those worldwide reported from mantle wedge peridotites (average values). N numbers of samples analyzed, n.p. not present.

Figure captions

Figure 1. (a) Distribution of ophiolitic rocks in the Eastern Desert of Egypt (after Shackleton, 1994). (b) Geological map of Abu Dahr ((modified from the Geologic Map of Baranis, Geological Survey of Egypt (1992), Scale, 1:250,000). Numbers indicate locations of the observation points sampled. (c) Thematic Mapper of Abu Dahr massif for possible lithological discrimination.

Figure 2. The paragenetic sequence for the Abu Dahr ophiolitic rocks and associated silicates, carbonates, oxides, and Ni-sulfides and native alloys. Mineral abbreviations: see Table 2.

Figure 3. Optical (a, b, g, h) and backscattered electrons (c-f, i) images showing microtextures of Abu Dahr peridotites. (a-c) Harzburgites showing a typical porphyroclastic texture, characterized by millimeter-sized porphyroclasts of olivine and orthopyroxene embedded in a fine-grained neoblastic matrix. Olivine occurs as small inclusions in orthopyroxene. Recrystallized grains of olivine usually rimming olivine and orthopyroxene porphyroclasts (0.5 cm). Unaltered chromite grain with orthopyroxene and amphibole inclusions. (d-f) Partially serpentinized harzburgites showing mesh-textures typical of serpentine (lizardite and/or chrysotile) forming mesh textures after olivine. Alongside serpentine, secondary brucite, magnetite, sulfides and native alloys, and are present. Brucite is developed in the centers of narrow veinlets during the initial serpentinization. (g-i) Atg-serpentinites consist of ~ 100% antigorite with an interlocking texture; (i) Zoned chromite grain up to 2 mm across commonly rimmed/fractured by secondary magnetite. Mineral abbreviations: Ol olivine, Opx orthopyroxene, Spl spinel, Brc brucite, Mag magnetite, Atg antigorite, Tlc talc, Mgs magnesite, Srp serpentine.

Figure 4. Backscattered electron (a-e) and optical (f) images showing textural characteristics of the pentlandite-rich assemblage in Abu Dahr serpentinized peridotites. (a) Individual grains of cobaltian pentlandite and magnetite in serpentine. (b) Euhedral grain of heazlewoodite encapsulating magmatic pentlandite relics. (c) Zoned euhedral grain of Ni-rich awaruite (native Ni) core rimmed by stoichiometric awaruite. (d, e) Large desulfurized pentlandite grains partly replaced and rimmed by awaruite. (f) Disseminated blebs, up to 50 µm in diameter, comprise a granular aggregate of godlevskite which is replaced by a reticulate pattern of lamellar millerite (veinlets ~ 5 µm in width), C.P. Numbers indicate the EMP point analyzed performed in the Tables 3 and 4. Mineral abbreviations: see Table 2.

Figure 5. Backscattered electron images showing textural-mineralogical characteristics of the godlevskite-rich assemblage in Abu Dahr serpentinized peridotites. (a) Composite intergrowths

of the godlevskite-rich assemblages in serpentine. Enlarged area is shown in (b). (b) Pentlandite intergrown with heazlewoodite, godlevskite, and magnetite. (c) Heazlewoodite intergrown with godlevskite and mantled by magnetite. (d) Enlarged area of box in c showing a BSE image of heazlewoodite replaced by godlevskite. Mineral abbreviations: see Table 2.

Figure 6. Backscattered electron images showing textural-mineralogical characteristics of the millerite-rich assemblage in Abu Dahr serpentinized peridotites. (a) Two composite grains with characteristic replacement textural patterns as a result of serpentinization. One shows replacement of cobaltian pentlandite by heazlewoodite, and the other showing complex replacement patterns of cobaltian pentlandite by heazlewoodite and millerite in talc-carbonate rocks. (b) Millerite intergrown with native Ni. Millerite rimmed by native Ni and nickeliferous goethite. Euhedral tabular goethite crystals surrounding millerite and scattered in serpentine. Numbers indicate the EMP point analyzed performed in the Tables 3 and 4. Mineral abbreviations: see Table 2.

Figure 7. (a) Compositional relationship between Fo content of olivine and Cr#s of coexisting Cr-spinels of mantle harzburgites of Abu Dahr; the olivine-spinel mantle array (OSMA) after Arai (1994). Fields for abyssal and forearc peridotites are from Dick and Bullen (1984), Parkinson and Pearce (1998), Pearce et al. (2000). FMM-fertile MORB mantle. (b) Plot of Mg# versus Cr# of Cr-spinels. Fields for abyssal peridotite is from Dick and Bullen (1984), the Mariana forearc field from Ishii et al. (1992). (c) Plot of $\Delta\log(fO_2)$ FMQ (fayalite-magnetite-quartz) versus Cr# in Cr-spinel for the Abu Dahr harzburgites. Discrimination boundaries for MOR dunite and harzburgite, and SSZ dunite and harzburgite are from Dare et al. (2009).

Figure 8. (a) Chemical composition (at.%) of the analyzed Ni-sulfides and awaruite-native Ni of the studied Abu Dahr peridotites on the Fe-Ni-S phase diagram (after Misra and Fleet, 1973). (b) Mineral stabilities in the ternary diagram Fe_9S_8-Ni_9S_8-Co_9S_8 (after Kaneda et al. 1986) with coexisting of the Abu Dahr pentlandites occupy the stability field at 200°C.

Figure 9. Binary plots (wt%) between the metals in Abu Dahr pentlandites compared with pentlandites from different localities worldwide (see text). (a) Co versus Ni, b) Co versus Fe, (c) Co versus Fe+Ni, and (d) Fe versus Co+Ni. Additional data are from Vourinos, Greece: Tzamos et al., 2016; Massif du Sud Peridotite Nappe, New Caledonia: Augé et al. 1999; Cemetery Ridge, Arizona: Haxel et al., 2018; Santa Elena Nappe, Costa Rica: Schwarzenbach et al., 2014; and Latao, SE Sulawesi: Rafianto et al., 2012.

Figure 10. Variation diagrams of Abu Dahr bulk rock MgO versus a) SiO_2, b) Al_2O_3, c) FeO_T, and d) CaO and compared with ultramafic rocks from other localities worldwide (see text). Additional data are from Mariana forearc: Parkinson and Pearce, 1998; Cemetery Ridge, Arizona: Haxel et al., 2018; and Santa Elena Nappe, Costa Rica: Schwarzenbach et al., 2014. PM primitive mantle (Palme and O'Neill, 2003). The arrows indicate the depletion trend of the samples.

Figure 11. Phase stability in the Fe-Ni-S-O-H system as a function of log fO_2 and log ΣS (activity of sulfur species) at 300°C and 2 KPa. The diagram illustrates stabilities for Ni minerals of interest in Abu Dahr serpentinites at 300°C and 2 kbar (after Frost, 1985). Red solid lines

mark boundaries between dominant Ni-sulfides-awaruite-magnetite of Abu Dahr. Blue solid lines mark boundaries between Fe-rich phases. Dashed lines are contours of log fS_2 in the fluid. Mineral abbreviations: see Table 2.

Figure 12. Pie charts showing the wt% proportions of Fe, Co, Ni, Cu, and S in Ni-sulfides and alloys of Abu Dahr comparable with those reported from mantle wedge serpentinites worldwide. Data sources are from Table S2 (supplementary material).

Table 1. GPS coordinates of the observation points (OP) sampled from Abu Dahr peridotites

Location sampled	OP	Latitudes North	Longitudes East	Nr of samples
Abu Dahr North	300	23° 36′ 36″	35° 04′ 38″	19
	301	23° 36′ 40″	35° 04′ 42″	8
	302	23° 36′ 41″	35° 05′ 53″	12
	303	23° 36′ 42″	35° 05′ 56″	9
	304	23° 36′ 40″	35° 05′ 57″	8
	305	23° 36′ 40″	35° 05′ 57″	17
Wadi Abu Khayl	306	23° 34′ 16″	35° 07′ 02″	24
	307	23° 34′ 29″	35° 04′ 59″	5
	308	23° 33′ 24″	35° 06′ 46″	25
	309	23° 33′ 21″	35° 06′ 49″	23
	310	23° 32′ 53″	35° 07′ 07″	2
	311	23° 33′ 03″	35° 07′ 15″	4
	312	23° 32′ 58″	35° 07′ 26″	4
	313	23° 32′ 57″	35° 07′ 26″	3
	314	23° 32′ 38″	35° 07′ 46″	3
	315	23° 32′ 44″	35° 07′ 54″	1
Wadi Abu Mastoura	316	23° 35′ 19″	35° 05′ 22″	20
	317	23° 35′ 10″	35° 05′ 28″	6
	318	23° 35′ 21″	35° 05′ 12″	16
	319	23° 35′ 32″	35° 04′ 54″	11
	320	23° 35′ 38″	35° 04′ 48″	3
	377	23° 35′ 10″	35° 05′ 48″	8
	378	23° 35′ 12″	35° 05′ 43″	3
	379	23° 35′ 22″	35° 05′ 21″	6
	380	23° 35′ 30″	35° 05′ 14″	4
	381	23° 35′ 31″	35° 05′ 08″	8
	382	23° 35′ 33″	35° 05′ 00″	6
	383	23° 35′ 41″	35° 04′ 39″	7
	384	23° 35′ 52″	35° 04′ 17″	2
Wadi Abu Sayyal	321	23° 34′ 01″	35° 00′ 53″	23
	322	23° 34′ 26″	35° 01′ 05″	15
	323	23° 34′ 22″	35° 01′ 28″	9
	324	23° 34′ 28″	35° 01′ 21″	17
	325	23° 34′ 40″	35° 01′ 38″	5
	326	23° 30′ 38″	35° 06′ 47″	5
	327	23° 30′ 38″	35° 06′ 46″	15
	328	23° 30′ 45″	35° 07′ 06″	4
	329	23° 31′ 09″	35° 08′ 00″	18
Gebel Abu Sayyal	330	23° 35′ 47″	35° 01′ 09″	34
	331	23° 35′ 43″	35° 01′ 13″	22

Table 2. Primary and secondary Ni-bearing phases in serpentinized peridotites of Abu Dahr with refering to mineral abbreviation used in this study

Primary Ni-bearing phases			Secondary Ni-bearing phases		
Mineral	Abbreviation	Stoichiometric formula	Mineral	Abbreviation	Stoichiometric formula
Pentlandite	Pn	$(Ni,Fe)_9S_8$	Heazlewoodite	Hzl	Ni_3S_2
Cobaltian pentlandite	CoPn	$(Ni,Fe,Co)_9S_8$	Godlevskite	Gv	Ni_9S_8
			Millerite	Mlr	NiS
			Chalcopyrite	Ccp	$CuFeS_2$
			Awaruite	Awr	Ni_3Fe
			Native Ni	native Ni	Ni
			Magnetite	Mag	Fe_3O_4
			Goethite	Gth	(Fe,Ni)OOH

Table 3. Representative EMP analyses of pentlandite Pn and cobaltian pentlandite Co Pn in Abu Dahr serpentinized peridotites

					Element wt%					Element at%				Mineral Formulas (apfu)				Ratios		
Sample	Figure	Point	Assemblage	Mineral	Fe	Co	Ni	S	Total	Fe	Co	Ni	S	Fe	Co	Ni	S	Ni/Co	Ni/Fe	Metal/S
316-3				Pn*	26.06	2.14	36.69	35.12	100	20.99	1.63	28.11	49.27	3.72	0.29	4.99	8.00	17.25	1.34	1.03
316-5				Pn*	27.95	1.96	34.58	35.51	100	22.44	1.49	26.43	49.66	4.01	0.27	4.72	8.00	17.74	1.18	1.01
322-16				Pn*	27.80	1.59	36.63	33.98	100	22.54	1.22	28.26	47.98	3.90	0.21	4.89	8.00	23.16	1.25	1.08
306-7				Pn*	26.69	2.72	35.25	35.33	100	21.46	2.07	26.97	49.49	3.82	0.37	4.81	8.00	13.03	1.26	1.02
				Average	*27.13*	*2.10*	*35.79*	*34.98*	100	*21.86*	*1.60*	*27.44*	*49.10*	*3.86*	*0.29*	*4.85*	*8.00*	*17.79*	*1.26*	*1.04*
				St.Dev.	*0.91*	*0.47*	*1.04*	*0.69*	*0.00*	*0.76*	*0.36*	*0.89*	*0.76*	*0.12*	*0.07*	*0.12*	*0.00*	*4.16*	*0.07*	*0.03*
306-7	4a	1		Co Pn*	25.57	5.17	36.85	32.41	100	20.96	4.02	28.74	46.28	3.51	0.67	4.82	8.00	7.15	1.37	1.16
306-7	4a	2		Co Pn*	26.23	5.28	35.51	32.98	100	21.59	4.12	27.81	46.48	3.63	0.69	4.68	8.00	6.75	1.29	1.15
306-7	4a	3		Co Pn*	24.91	5.00	35.68	34.41	100	20.16	3.83	27.48	48.53	3.52	0.67	4.81	8.00	7.17	1.36	1.06
309-5	6a	15	Pn-Hzl-Mag	Co Pn	25.54	5.10	34.36	35.00	100	20.59	3.90	26.36	49.16	3.64	0.69	4.67	8.00	6.76	1.28	1.03
309/5			Pn-Hzl-Mag	Co Pn	24.84	5.04	36.30	33.82	100	20.18	3.88	28.06	47.87	3.48	0.67	4.85	8.00	7.23	1.39	1.09
322-7A	5b	7	Pn-Hzl-Gv-Mag	Co Pn	25.57	5.17	35.12	34.14	100	20.73	3.97	27.09	48.21	3.60	0.69	4.71	8.00	6.82	1.31	1.07
322-7A			Pn-Hzl-Gv-Mag	Co Pn	23.15	6.22	36.72	33.91	100	18.81	4.79	28.39	48.00	3.25	0.83	4.92	8.00	5.93	1.51	1.08
309-5	6a	17	Pn-Hzl-Mlr.	Co Pn	24.66	6.28	35.57	33.49	100	20.08	4.85	27.56	47.51	3.44	0.83	4.73	8.00	5.68	1.37	1.10
309-5	6a	18	Pn-Hzl-Mlr.	Co Pn	22.39	7.53	36.17	33.91	100	18.20	5.80	27.98	48.02	3.15	1.00	4.85	8.00	4.82	1.54	1.08
				Average	*24.76*	*5.64*	*35.81*	*33.79*	100	*20.14*	*4.35*	*27.72*	*47.78*	*3.47*	*0.75*	*4.78*	*8.00*	*6.48*	*1.38*	*1.09*
				St.Dev.	*1.24*	*0.86*	*0.79*	*0.76*	*0.00*	*1.05*	*0.67*	*0.71*	*0.92*	*0.17*	*0.11*	*0.09*	*0.00*	*0.83*	*0.09*	*0.04*

Notes: *discrete individual mineral

Table 4. Representative EMP analyses of heazlewoodite Hzl, godlevskite Gv, millerite Mlr, chalcopyrite Ccp, awaruite Awr, and native Ni in Abu Dahr serpentinized–carbonated peridotites

					Element wt%						Element at%					Mineral Formulas (apfu)					
Sample	Figure	Point	Assemblage	Mineral	Fe	Co	Ni	Cu	S	Total	Fe	Co	Ni	Cu	S	Fe	Co	Ni	Cu	S	Metal/S
306-7	4b	4		Hzl*	0.40	0.00	70.36	0.00	29.24	100	0.34	0.00	56.64	0.00	43.09	0.02	0.00	2.98	0.00	2.00	1.32
306-7				Hzl*	0.39	0.00	71.19	0.00	28.42	100	0.33	0.00	57.62	0.00	42.10	0.02	0.00	2.98	0.00	2.00	1.38
322-7A	6a	16	Pn-Hzl-Mag	Hzl	0.41	0.00	71.77	0.00	27.58	100	0.35	0.00	58.38	0.00	41.41	0.02	0.00	2.98	0.00	2.00	1.42
322-7A	5a	19	Pn-Hzl-Mlr	Hzl	0.51	0.00	72.40	0.00	26.75	100	0.44	0.00	59.17	0.00	40.52	0.02	0.00	2.98	0.00	2.00	1.47
322-7A	5b	8	Pn-Hzl-Gv-Mag	Hzl	1.87	0.00	71.16	0.00	26.91	100	1.61	0.00	58.12	0.00	40.32	0.08	0.00	2.92	0.00	2.00	1.48
322-7A	5d	13	Hzl-Gv-Mag	Hzl	3.60	0.00	70.15	0.00	26.25	100	3.11	0.00	57.61	0.00	39.46	0.15	0.00	2.85	0.00	2.00	1.54
322-7A	5a	11	Pn-Hzl-Gv-Mag	Hzl	3.78	0.00	68.99	0.00	27.23	100	3.24	0.00	56.28	0.00	40.66	0.16	0.00	2.84	0.00	2.00	1.46
				Average	*1.57*	*0.00*	*70.86*	*0.00*	*27.48*	*100*	*1.35*	*0.00*	*57.69*	*0.00*	*41.08*	*0.07*	*0.00*	*2.93*	*0.00*	*2.00*	*1.44*
				St.Dev.	*1.54*	*0.00*	*1.13*	*0.00*	*1.04*		*1.33*	*0.00*	*1.00*	*0.00*	*1.22*	*0.06*	*0.00*	*0.06*	*0.00*	*0.00*	*0.07*
322-7A	5b	9	Hzl-Gv-Mag	Gv	2.33	0.00	67.57	0.00	29.71	100	1.96	0.00	54.10	0.00	44.06	0.31	0.00	8.69	0.00	8.00	1.27
322-7A	5a	10	Pn-Hzl-Gv-Mag	Gv	2.44	0.00	66.32	0.00	29.92	99	2.04	0.00	52.77	0.00	45.31	0.33	0.00	8.67	0.00	8.00	1.21
322-7A	5b	12	Pn-Hzl-Gv-Mag	Gv	1.59	0.16	68.42	0.00	29.34	100	1.33	0.13	54.78	0.00	43.68	0.21	0.02	8.77	0.00	8.00	1.29
322-7A	5d	14	Pn-Hzl-Gv-Mag	Gv	1.31	0.20	67.60	0.00	30.89	100	1.10	0.16	53.82	0.00	45.03	0.18	0.03	8.79	0.00	8.00	1.22
				Average	*1.92*	*0.09*	*67.48*	*0.00*	*29.97*	*99*	*1.61*	*0.07*	*53.87*	*0.00*	*44.52*	*0.26*	*0.01*	*8.73*	*0.00*	*8.00*	*1.25*
				St.Dev.	*0.55*	*0.11*	*0.86*	*0.00*	*0.66*		*0.46*	*0.08*	*0.84*	*0.00*	*0.77*	*0.07*	*0.02*	*0.06*	*0.00*	*0.00*	*0.04*
309-5	6b	23	Mlr-native Ni-Gth	Mlr	0.44	0.00	66.00	0.00	33.55	100	0.36	0.00	49.44	0.00	50.25	0.01	0.00	0.99	0.00	1.00	0.99
309-5				Mlr	0.47	0.00	64.08	0.00	35.46	100	0.38	0.00	48.37	0.00	51.20	0.01	0.00	0.99	0.00	1.00	0.95
309-5				Mlr	0.78	0.00	64.21	0.00	35.01	100	0.64	0.00	49.73	0.00	49.63	0.01	0.00	0.99	0.00	1.00	1.01
309-5				Mlr	0.83	0.12	64.16	0.00	34.89	100	0.67	0.00	48.59	0.00	50.54	0.01	0.00	0.98	0.00	1.00	0.97
322-7A	6a	20	Pn-Hzl-Mlr	Mlr	0.53	0.32	64.46	1.79	33.02	100	0.44	0.26	49.83	1.31	48.08	0.01	0.00	0.96	0.03	1.00	1.08
322-7A	6a	21	Pn-Hzl-Mlr	Mlr	0.85	0.35	65.13	0.57	33.10	100	0.70	0.27	51.10	0.41	47.54	0.01	0.01	0.97	0.01	1.00	1.10
				Average	*0.65*	*0.13*	*64.67*	*0.39*	*34.17*	*100*	*0.53*	*0.09*	*49.51*	*0.29*	*49.54*	*0.01*	*0.00*	*0.98*	*0.01*	*1.00*	*1.02*
				St.Dev.	*0.19*	*0.16*	*0.75*	*0.72*	*1.07*		*0.15*	*0.14*	*0.98*	*0.53*	*1.44*	*0.00*	*0.00*	*0.01*	*0.01*	*0.00*	*0.06*
322-7A	6a	22	Pn-Hzl-Mlr	Ccp	29.60	0.00	1.49	33.67	35.25	100	24.28	0.00	1.16	24.27	50.37	0.98	0.00	0.05	0.98	2.00	0.99
				Average	*29.60*	*0.00*	*1.49*	*33.67*	*35.25*	100	24.28	0.00	1.16	24.27	50.37	*0.98*	*0.00*	*0.05*	*0.98*	*2.00*	*0.99*
306-7	4c	5	Awr-native Ni	Awr (rim)	21.76	1.15	76.41	0.11	0.00	99	22.61	1.14	76.10	0.12	0.00	22.61	1.14	76.10	0.10	0.00	0.00
306-7	4c	6	Awr-native Ni	Awr (core)	13.45	0.96	85.03	0.33	0.00	100	14.06	0.95	84.76	0.30	0.00	14.06	0.95	84.76	0.31	0.00	0.00
				Average	*17.61*	*1.06*	*80.72*	*0.22*	*0.00*	*100*	*18.34*	*1.04*	*80.43*	*0.21*	*0.00*	*18.34*	*1.04*	*80.43*	*0.21*	*0.00*	*0.00*
309-5	6b	24	Mlr-native Ni-Gth	native Ni	4.96	0.39	92.46	2.13	0.00	100	5.19	0.41	91.16	2.00	0.00						0.00
309-5			Mlr-native Ni-Gth	native Ni	6.23	0.46	91.88	1.44	0.00	100	6.55	0.47	91.58	1.35	0.00						0.00
309-5			Mlr-native Ni-Gth	native Ni	4.84	0.31	92.75	2.09	0.00	100	4.95	0.30	92.57	1.88	0.00						0.00
309-5				native Ni	6.28	0.57	91.70	1.45	0.00	100	6.87	0.59	90.64	1.40	0.00						0.00
				Average	*5.58*	*0.43*	*92.20*	*1.78*	*0.00*	*100*	*5.89*	*0.44*	*91.49*	*1.66*	*0.00*						*0.00*
				St.Dev.	*0.78*	*0.11*	*0.49*	*0.38*	*0.00*		*0.96*	*0.12*	*0.82*	*0.33*	*0.00*						*0.00*

Notes: *discrete individual mineral

Table 5. Representative EMP analyses and Ni contents (ppm) of magnetite Mag, ferritchromite Fe-chromite and goethite Gth from Abu Dahr serpentinized peridotites

Sample	Mineral	SiO_2 wt%	TiO_2 wt%	Al_2O_3 wt%	Cr_2O_3 wt%	FeO_{Total} wt%	MgO wt%	MnO wt%	CaO wt%	NiO wt%	Total wt%	Ni ppm
318-9	Mag	0.49	0.05	0.06	7.75	83.9	0.93	0.19	0.11	0.40	93.90	3142
318-9	Mag	0.38	0.03	0.00	5.72	83.9	0.88	0.00	0.00	0.45	91.39	3535
319-8	Mag	1.03	0.01	0.00	1.45	82.4	0.90	0.10	0.02	1.24	87.16	9741
319-8	Mag	0.78	0.00	0.34	3.52	83.9	1.19	0.03	0.03	0.67	90.46	5263
319-8	Mag	0.53	0.00	0.09	4.52	84.5	0.87	0.11	0.07	1.05	91.73	8248
319-8	Mag	0.80	0.00	0.15	5.92	81.2	1.53	0.00	0.05	0.77	90.46	6049
331-19	Mag	1.03	0.28	0.00	0.17	88.8	0.44	0.11	0.02	0.70	91.59	5499
331-19	Mag	1.21	0.00	0.01	0.00	86.3	1.79	0.00	0.08	0.60	89.96	4713
331-19	Mag	0.84	0.03	0.00	4.65	85.2	0.91	0.00	0.00	0.88	92.53	6913
	Average	*0.79*	*0.04*	*0.07*	*3.74*	*84.47*	*1.05*	*0.06*	*0.04*	*0.75*	*91.02*	*5900*
318-9	Fe-chromite	0.82	0.02	2.72	31.79	57.3	3.03	0.42	0.01	0.78	96.88	6127
318-9	Fe-chromite	0.87	0.06	0.69	28.76	61.8	1.62	0.66	0.03	0.91	95.40	7148
318-9	Fe-chromite	0.85	0.13	1.06	31.00	58.9	2.11	0.54	0.02	0.41	95.03	3221
319-8	Fe-chromite	0.86	0.08	0.16	12.71	76.0	0.99	0.25	0.07	1.19	92.34	9348
330-9	Fe-chromite	0.90	0.01	0.23	19.81	68.9	0.84	0.39	0.07	0.94	92.06	7384
330-9	Fe-chromite	0.91	0.00	0.84	26.09	60.6	1.53	0.82	0.05	0.44	91.28	3456
330-9	Fe-chromite	0.89	0.00	0.81	27.99	56.9	1.40	0.82	0.09	0.24	89.12	1885
330-9	Fe-chromite	0.86	0.00	0.65	30.50	56.9	1.97	0.84	0.09	0.33	92.11	2592
330-9	Fe-chromite	0.86	0.02	0.12	17.68	71.8	1.34	0.15	0.00	0.71	92.64	5577
331-19	Fe-chromite	0.87	0.13	3.21	32.46	53.9	2.89	0.47	0.01	0.38	94.33	2985
	Average	*0.87*	*0.05*	*1.05*	*25.88*	*62.29*	*1.77*	*0.54*	*0.04*	*0.63*	*93.12*	*4973*
309-5	Gth					59.3				1.91	61.22	15004
309-5	Gth					62.2				2.12	64.33	16654
	Average					*60.76*				*2.02*	*62.78*	*15829*

Notes: ppm Ni = wt% NiO*10000/1.273

Table 6. Calculated equilibrium P–T and oxygen fugacities for Abu Dahr harzburgites

Lithology	Harzburgite											
Sample	316-3-1	316-3-2	316-3-3	316-3-4	316-3-5	316-3-6	316-5-1	316-5-2	316-5-3	316-5-4	318-9-1	318-9-2
	Spinel											
Cr#	60.0	61.1	64.1	63.2	63.8	63.5	65.3	64.6	62.1	60.0	65.3	65.0
Mg#	55.7	56.7	54.9	55.1	55.4	56.2	57.7	57.5	56.0	57.9	42.8	46.0
Fe3+#	5.1	5.0	4.9	4.1	4.5	4.5	4.4	4.8	4.5	5.0	6.0	6.3
XFe^{2+}	0.443	0.433	0.451	0.449	0.446	0.438	0.423	0.425	0.440	0.421	0.572	0.5
XFe^{3+}	0.051	0.050	0.049	0.041	0.045	0.045	0.044	0.048	0.045	0.050	0.060	0.1
XAl	0.380	0.369	0.342	0.352	0.345	0.348	0.332	0.336	0.362	0.380	0.326	0.3
	Olivine											
Fo	91.6	91.3	91.5	91.9	91.7	91.7	92.2	91.1	91.2	91.4	91.66	91.9
XFe	0.084	0.087	0.084	0.080	0.081	0.081	0.077	0.089	0.087	0.085	0.082	0.080
	Orthopyroxene											
Mg#	92.0	91.8	92.0	91.7	91.9	92.3	92.3	92.0	91.9	92.1	91.9726	92.0331
XFe	0.080	0.082	0.080	0.083	0.081	0.077	0.077	0.080	0.081	0.079	0.080	0.080
	Clinopyroxene											
Mg#	94.1	94.8	95.2	94.2	94.2	94.9	95.2	94.6	94.5	94.6	98.0464	97.9853
XFe	0.059	0.052	0.048	0.058	0.058	0.051	0.048	0.054	0.055	0.054	0.01954	0.02015
T1 ℃	1193	1224	1168	1123	1174	1242	1195	1192	1179	1193	1219	1066
T2 ℃	1062	1097	1034	987	1042	1114	1062	1060	1047	1061	1091	925
T3 ℃	1205	1204	1143	1162	1191	1217	1169	1185	1181	1186	1054	910
TK	1478	1477	1416	1435	1464	1490	1442	1458	1454	1459	1327	1183
T4 ℃	927	971	875	884	916	882	970	920	913	923	918	920
P (KPar)	4.7	4.1	4.8	5.3	7.8	6.9	4.1	5.6	6.7	5.8	5.6	5.4
$Log(fO_2)^{FMQ}$	0.71	0.56	0.60	0.43	0.55	0.54	0.54	0.41	0.41	0.60	0.67	1.20

Note: Spl—spinel; Ol Fo—olivine forsterite; Opx—orthopyroxene; Cpx—clinopyroxene; XFe2+=Fe2+/(Fe2+Mg); XFe3+=Fe3/(Fe2+Fe3); XAl=Al(Al+Cr+Fe3); Fe3+#=Fe3+/(Fe3++Cr+Al)

T1, T2, and T3 are the equilibrium temperatures calculated using two-pyroxene geothermometers of Wood and Banno (1973),Wells (1977), and Brey and Köhler (1990), respectively.

T4 is the equilibrium temperatures calculated using Ca-in-Opx geothermometer of Brey and Köhler (1990).TK adopted from T3 of Brey and Köhler, 1990) for oxygen fugacity calculations. P (KPar) of Putirka (2008).

Oxygen fugacity (fO2) was determined using the oxybarometry of Ballhaus et al. (1991). Pressure of 1 GPa is assumed throughout. FMQ—fayalite-magnetite-quartz.

Table 7. Whole-rock major oxides (wt%) normalized on a volatile-free basis and trace elements (ppm) contents of Abu Dahr serpentinized harzburgites.

Sample	379/5	381/3	322/3	324/4	329/11
Normalized wt%					
SiO_2	42.12	43.91	45.02	44.33	46.92
TiO_2	0.01	0.01	0.01	0.04	0.06
Al_2O_3	0.65	0.41	0.53	0.90	0.73
FeO_{Total}	10.02	8.74	8.71	8.85	10.54
FeO	9.02	7.86	7.84	7.96	9.48
MnO	0.14	0.13	0.15	0.13	0.15
MgO	46.83	46.52	43.74	44.24	41.24
CaO	0.20	0.27	1.83	1.49	0.34
K_2O	0.00	0.00	0.00	0.00	0.01
Na_2O	0.00	0.00	0.00	0.00	0.00
P_2O_5	0.02	0.01	0.01	0.01	0.01
Total	100.00	100.00	100.00	100.00	100.00
LOI	10.7	9.66	11.83	9.22	12.71
Mg#	90	91	91	91	89
ppm					
Sc	0.00	13.70	0.00	0.00	0.00
V	29.00	23.40	23.00	31.70	32.90
Cr	7849.00	2461.30	2607.90	2468.80	3649.10
Co	143.90	127.80	119.10	121.70	122.70
Ni	2589.50	2378.60	2198.40	2246.60	1489.10
Cu	7.20	0.10	4.20	5.20	10.90
Zn	64.10	54.50	54.00	52.10	60.70
Ga	0.00	0.00	0.00	0.00	0.00
Rb	0.00	2.40	3.80	5.00	5.50
Sr	2.26	0.00	14.57	7.62	15.72
Y	3.80	6.10	6.00	6.30	4.90
Zr	0.00	28.90	0.00	29.40	35.60
Nb	0.00	0.00	0.00	0.00	0.00
Cs	18.00	0.00	0.00	0.00	46.60
Ba	0.00	0.00	0.00	0.00	0.00
La	0.00	0.00	0.00	0.00	0.00
Ce	0.00	0.00	0.00	0.00	0.00
Pr	0.00	0.00	0.00	5.70	0.00
Hf	0.00	0.00	0.00	0.00	0.00
Ta	0.00	0.00	0.00	0.00	0.00
Pb	0.00	0.00	0.00	0.00	0.00
Th	15.10	14.90	10.80	12.50	13.80
U	0.00	0.00	0.00	0.00	0.00

Notes: Mg# = (100*MgO/40.32)/(MgO/40.32+FeO/71.85)

This is the peer-reviewed, final accepted version for American Mineralogist, published by the Mineralogical Society of America.
The published version is subject to change. Cite as Authors (Year) Title. American Mineralogist, in press.
DOI: https://doi.org/10.2138/am-2022-8217. http://www.minsocam.org/

Figure 1

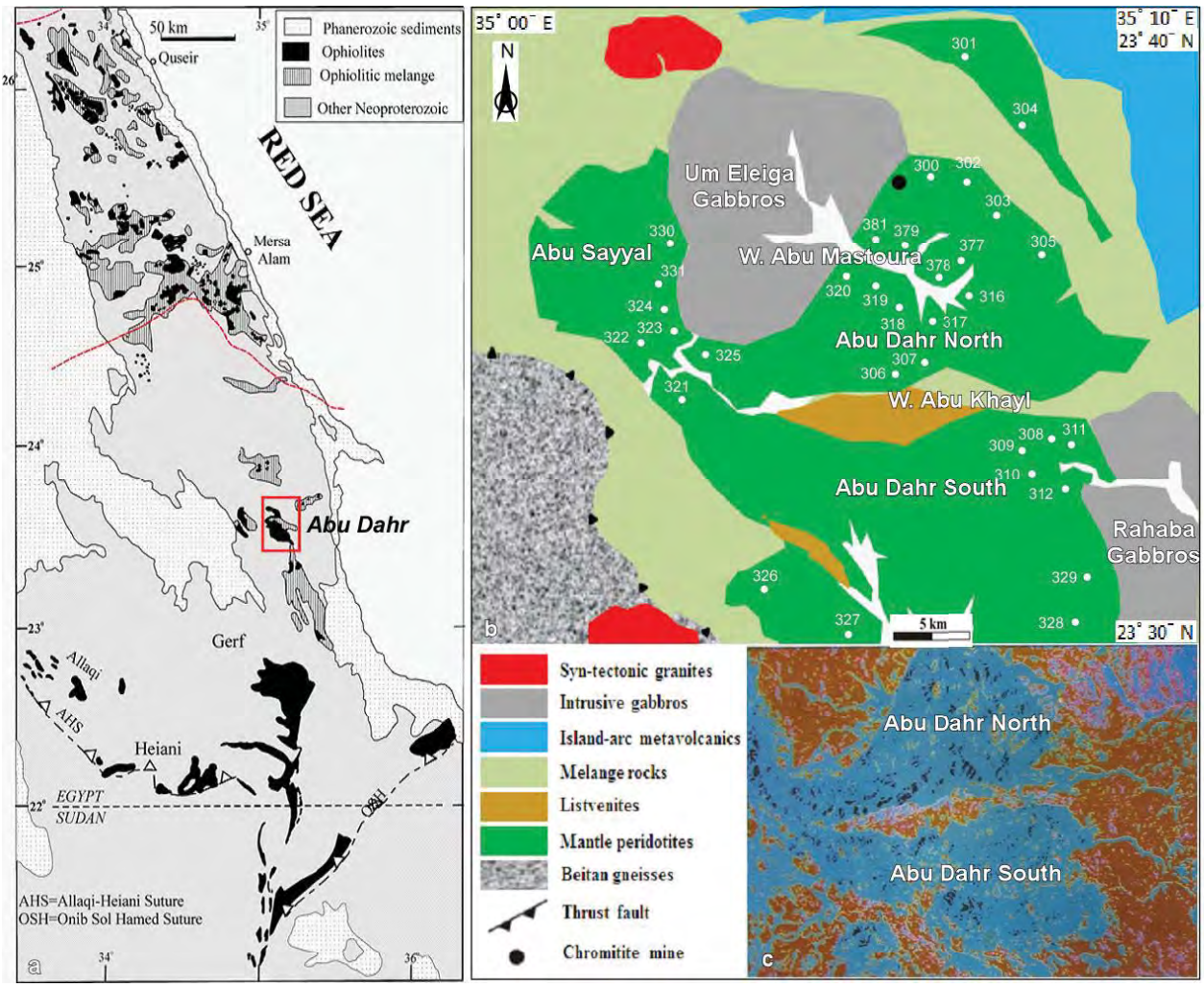

Figure 2

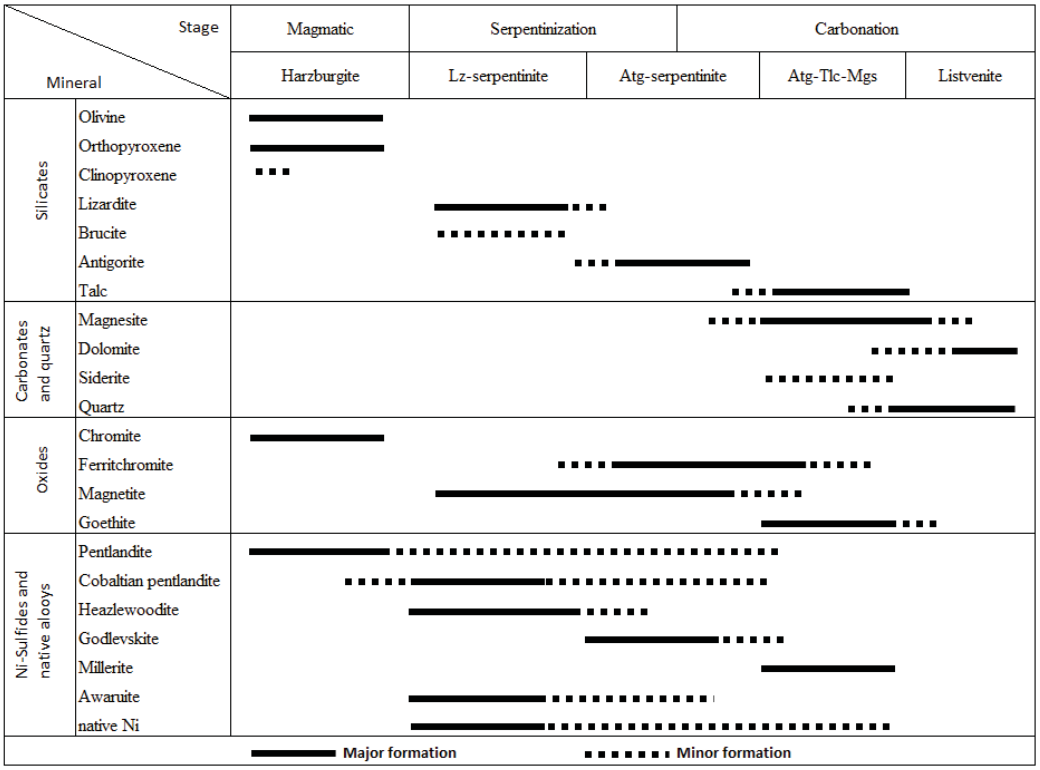

This is the peer-reviewed, final accepted version for American Mineralogist, published by the Mineralogical Society of America.
The published version is subject to change. Cite as Authors (Year) Title. American Mineralogist, in press.
DOI: https://doi.org/10.2138/am-2022-8217. http://www.minsocam.org/

Figure 3

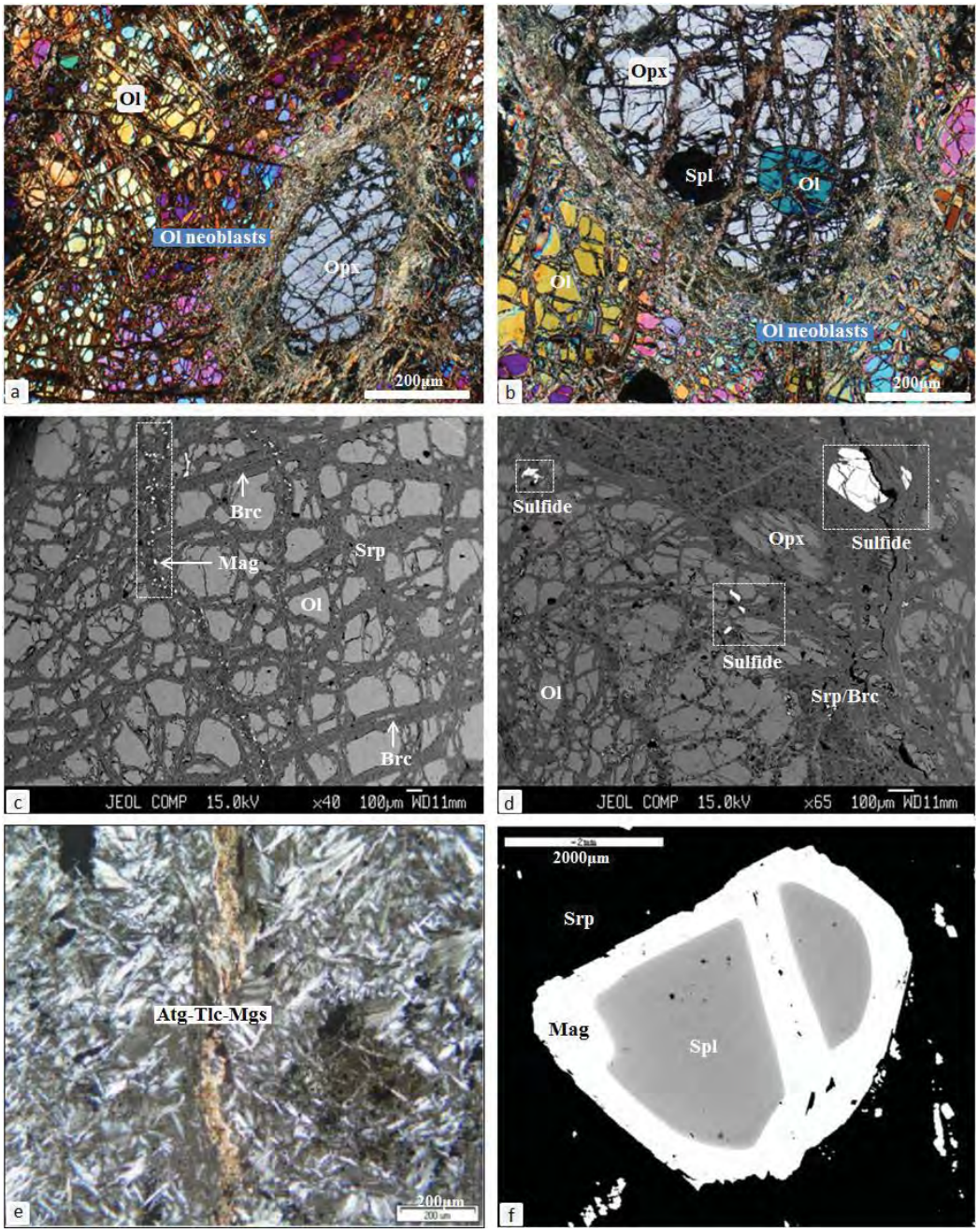

This is the peer-reviewed, final accepted version for American Mineralogist, published by the Mineralogical Society of America.
The published version is subject to change. Cite as Authors (Year) Title. American Mineralogist, in press.
DOI: https://doi.org/10.2138/am-2022-8217. http://www.minsocam.org/

Figure 4

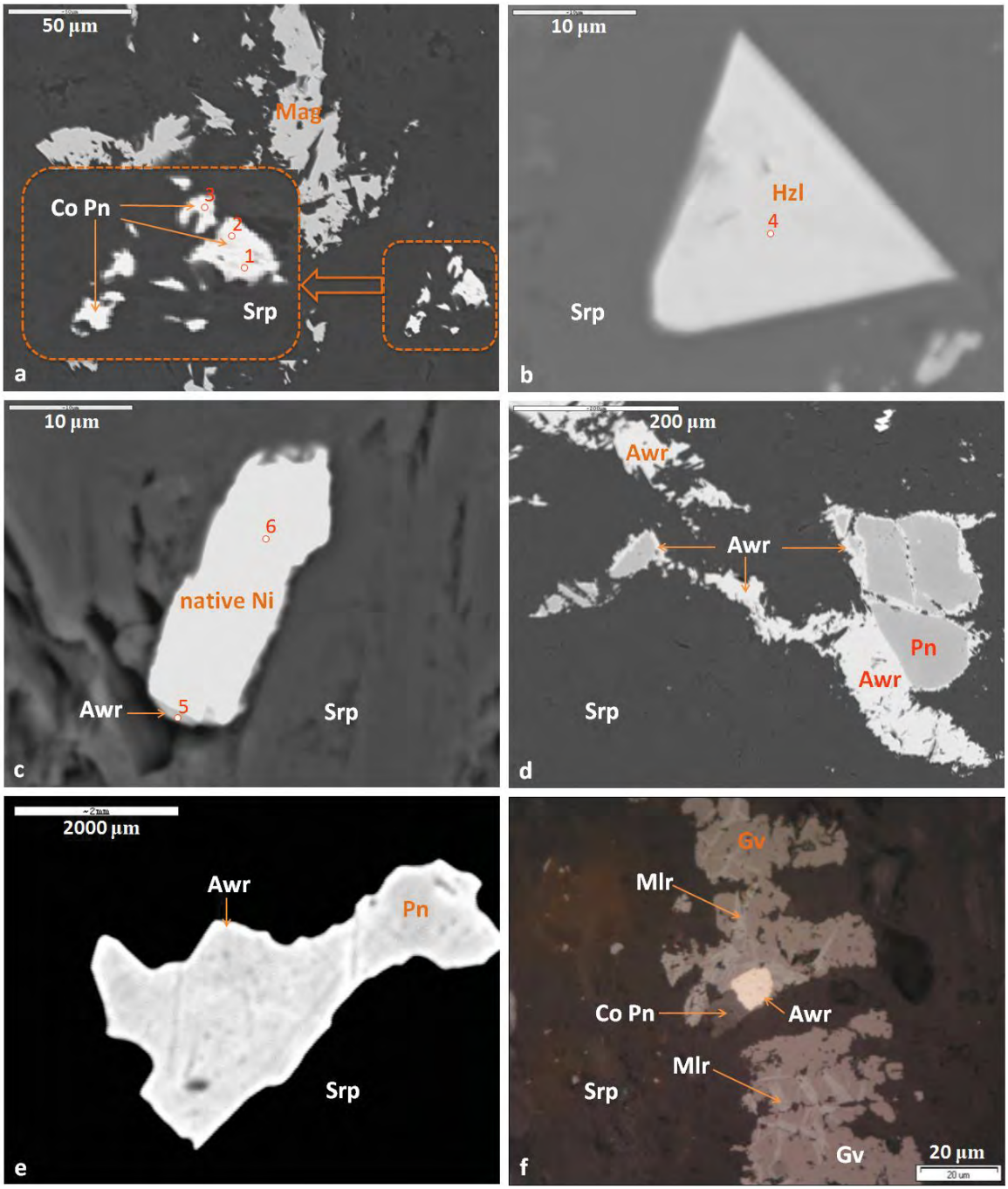

This is the peer-reviewed, final accepted version for American Mineralogist, published by the Mineralogical Society of America.
The published version is subject to change. Cite as Authors (Year) Title. American Mineralogist, in press.
DOI: https://doi.org/10.2138/am-2022-8217. http://www.minsocam.org/

Figure 5

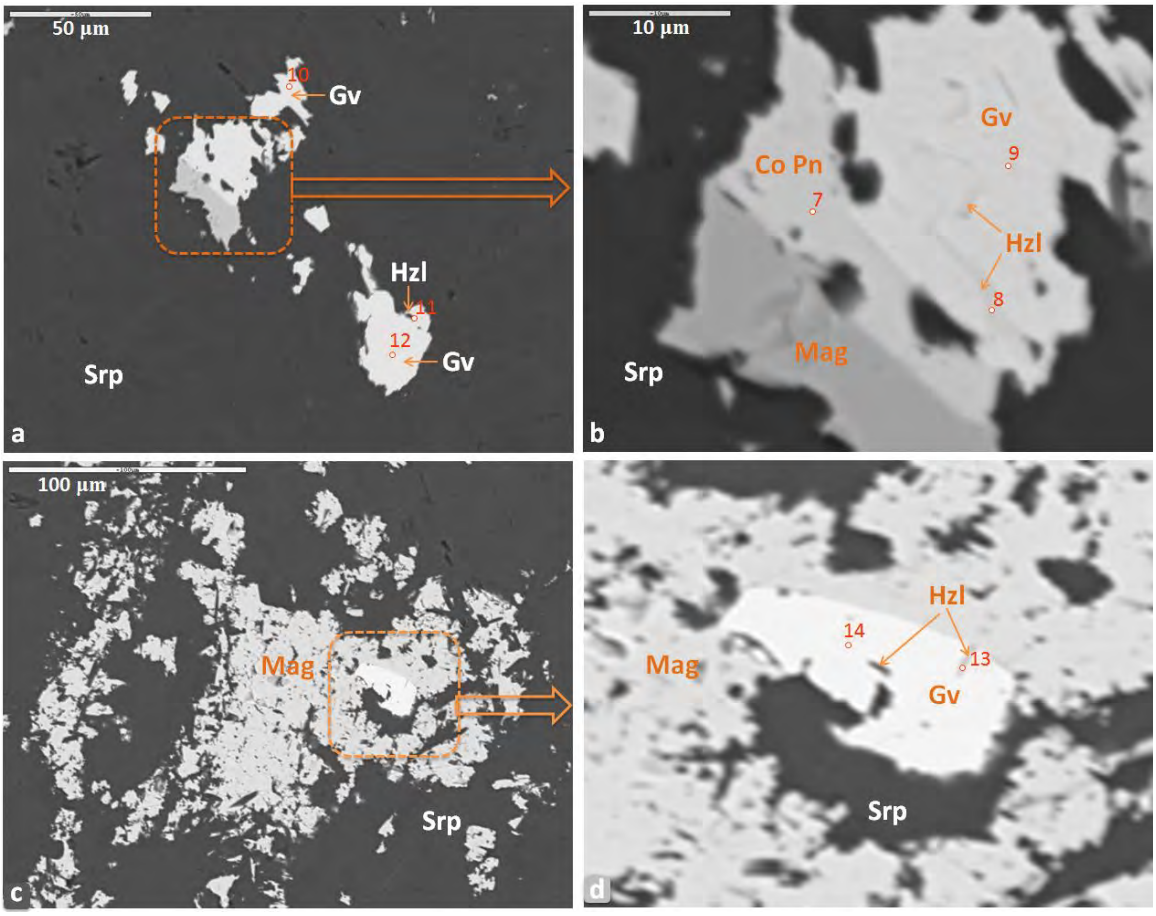

This is the peer-reviewed, final accepted version for American Mineralogist, published by the Mineralogical Society of America.
The published version is subject to change. Cite as Authors (Year) Title. American Mineralogist, in press.
DOI: https://doi.org/10.2138/am-2022-8217. http://www.minsocam.org/

Figure 6

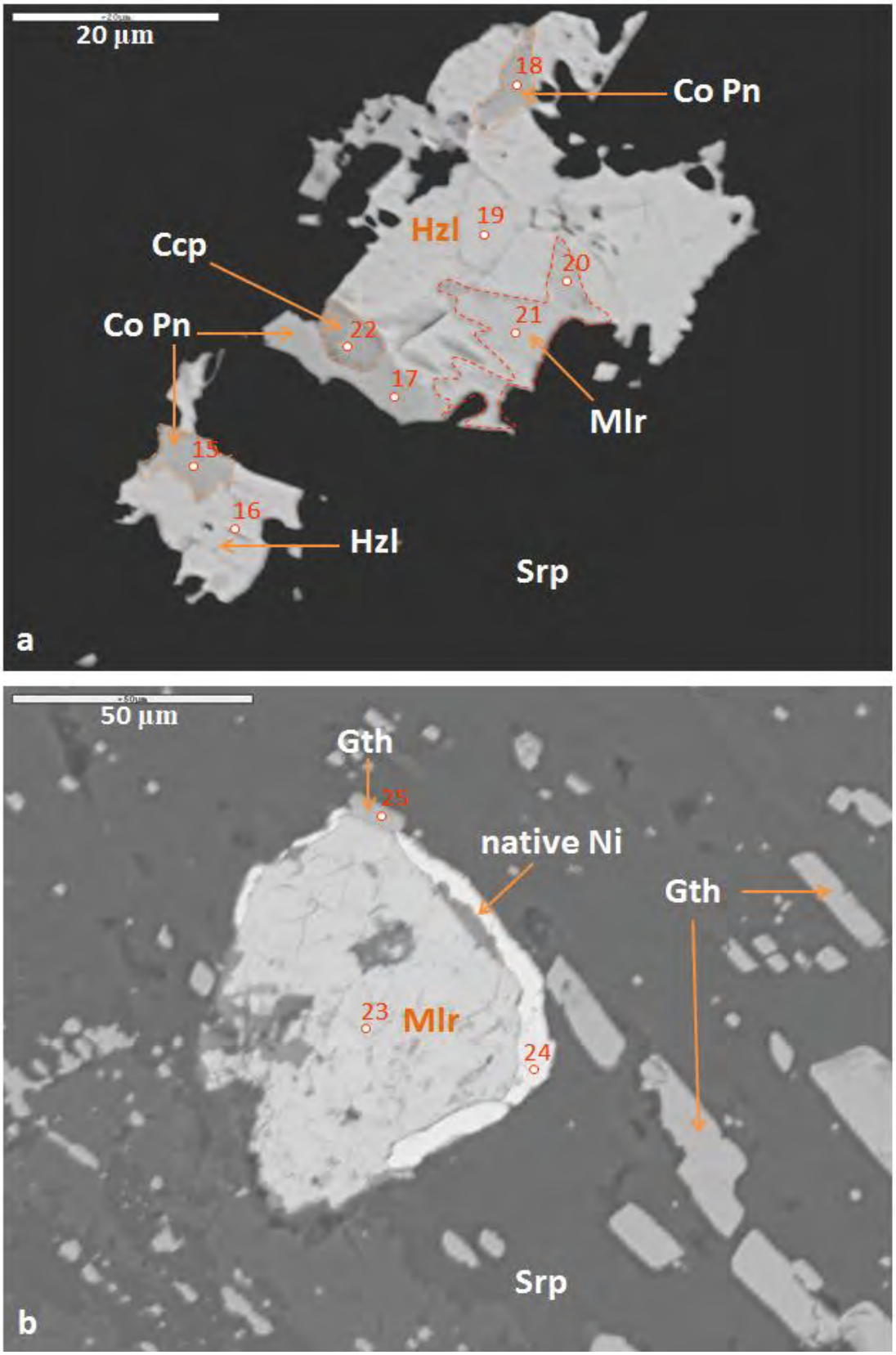

This is the peer-reviewed, final accepted version for American Mineralogist, published by the Mineralogical Society of America.
The published version is subject to change. Cite as Authors (Year) Title. American Mineralogist, in press.
DOI: https://doi.org/10.2138/am-2022-8217. http://www.minsocam.org/

Figure 7

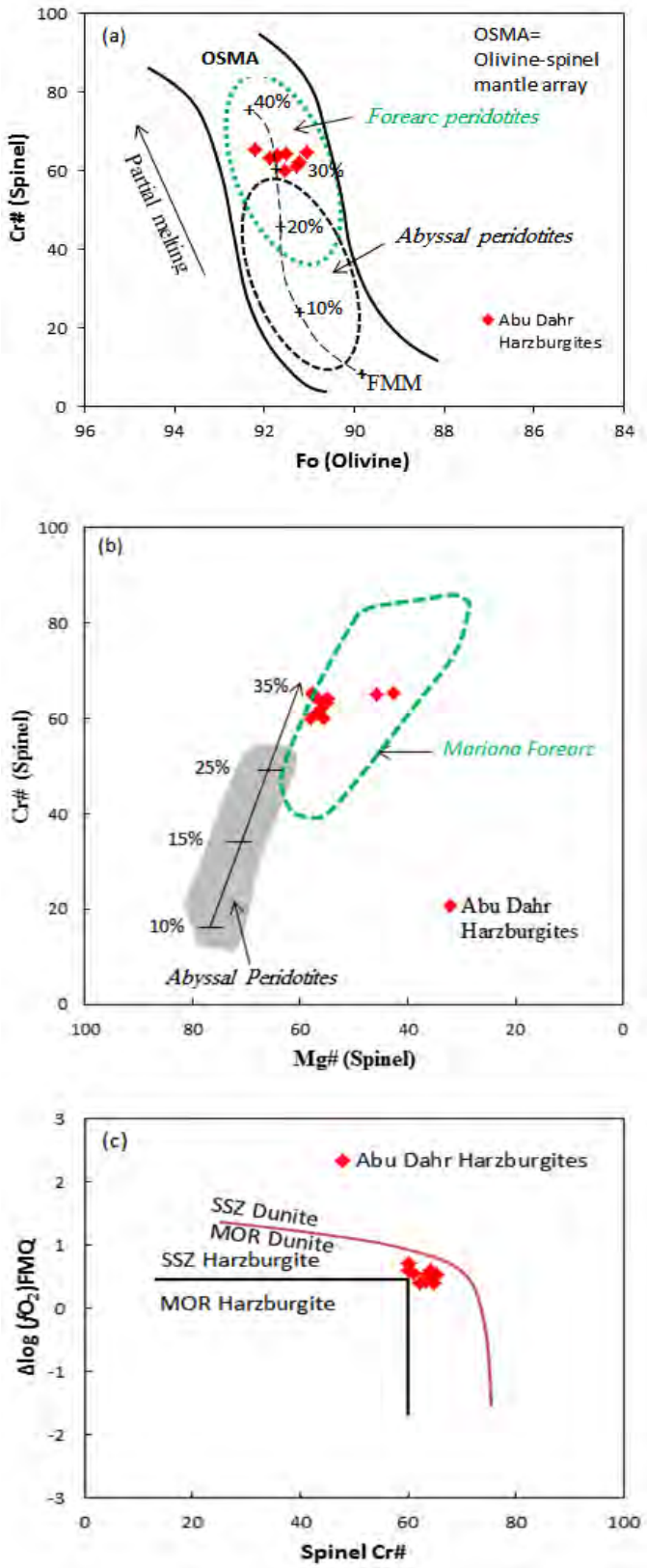

This is the peer-reviewed, final accepted version for American Mineralogist, published by the Mineralogical Society of America.
The published version is subject to change. Cite as Authors (Year) Title. American Mineralogist, in press.
DOI: https://doi.org/10.2138/am-2022-8217. http://www.minsocam.org/

Figure 8

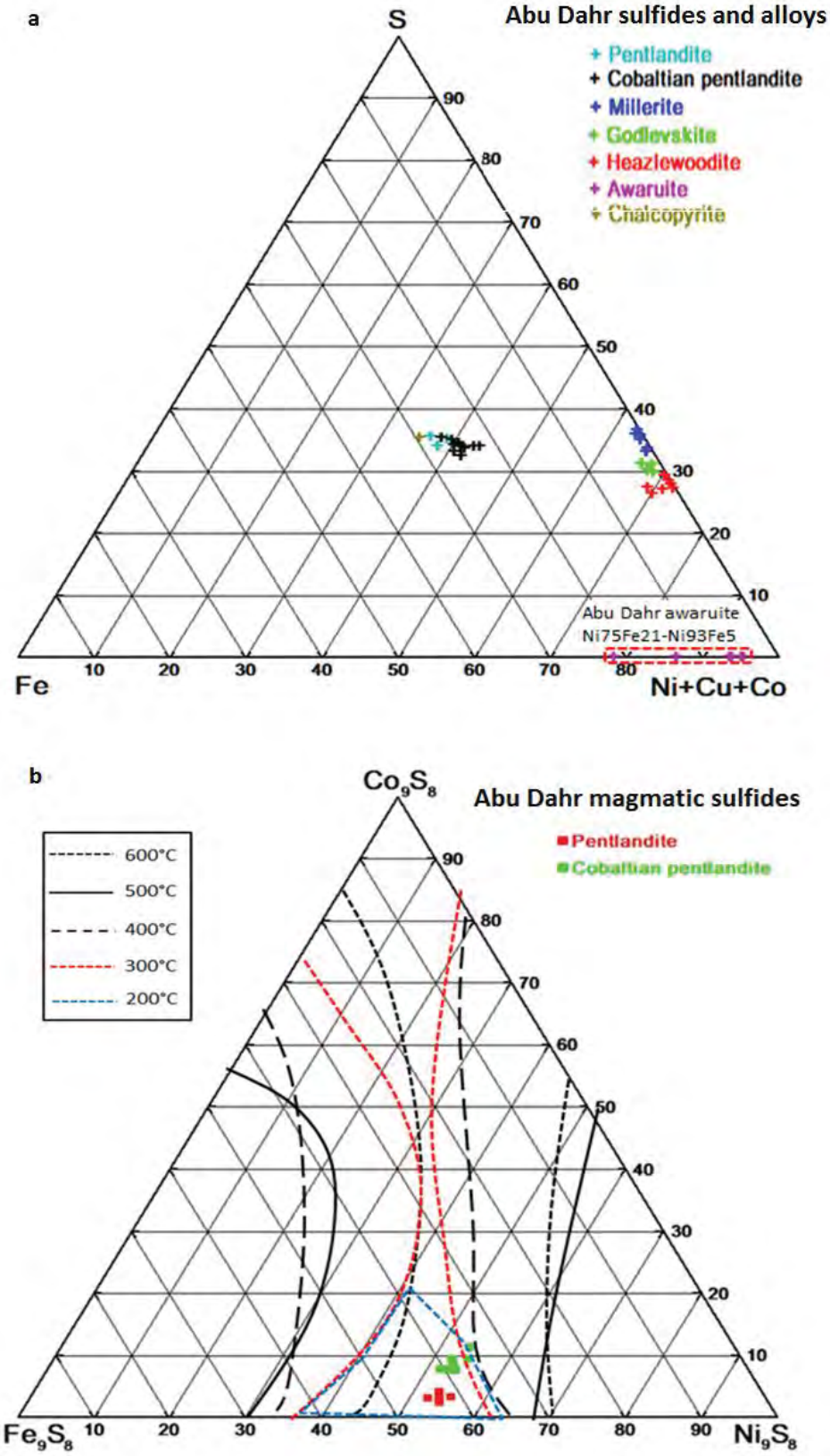

This is the peer-reviewed, final accepted version for American Mineralogist, published by the Mineralogical Society of America.
The published version is subject to change. Cite as Authors (Year) Title. American Mineralogist, in press.
DOI: https://doi.org/10.2138/am-2022-8217. http://www.minsocam.org/

Figure 9

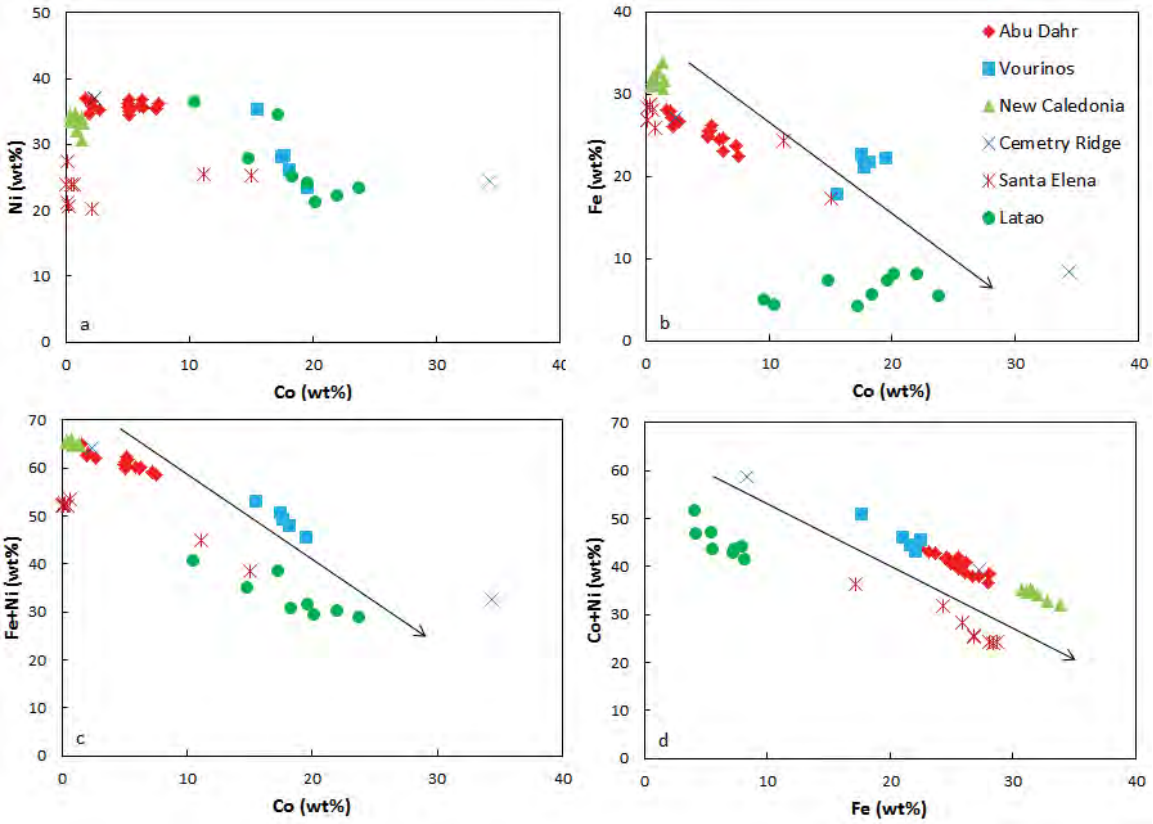

This is the peer-reviewed, final accepted version for American Mineralogist, published by the Mineralogical Society of America.
The published version is subject to change. Cite as Authors (Year) Title. American Mineralogist, in press.
DOI: https://doi.org/10.2138/am-2022-8217. http://www.minsocam.org/

Figure 10

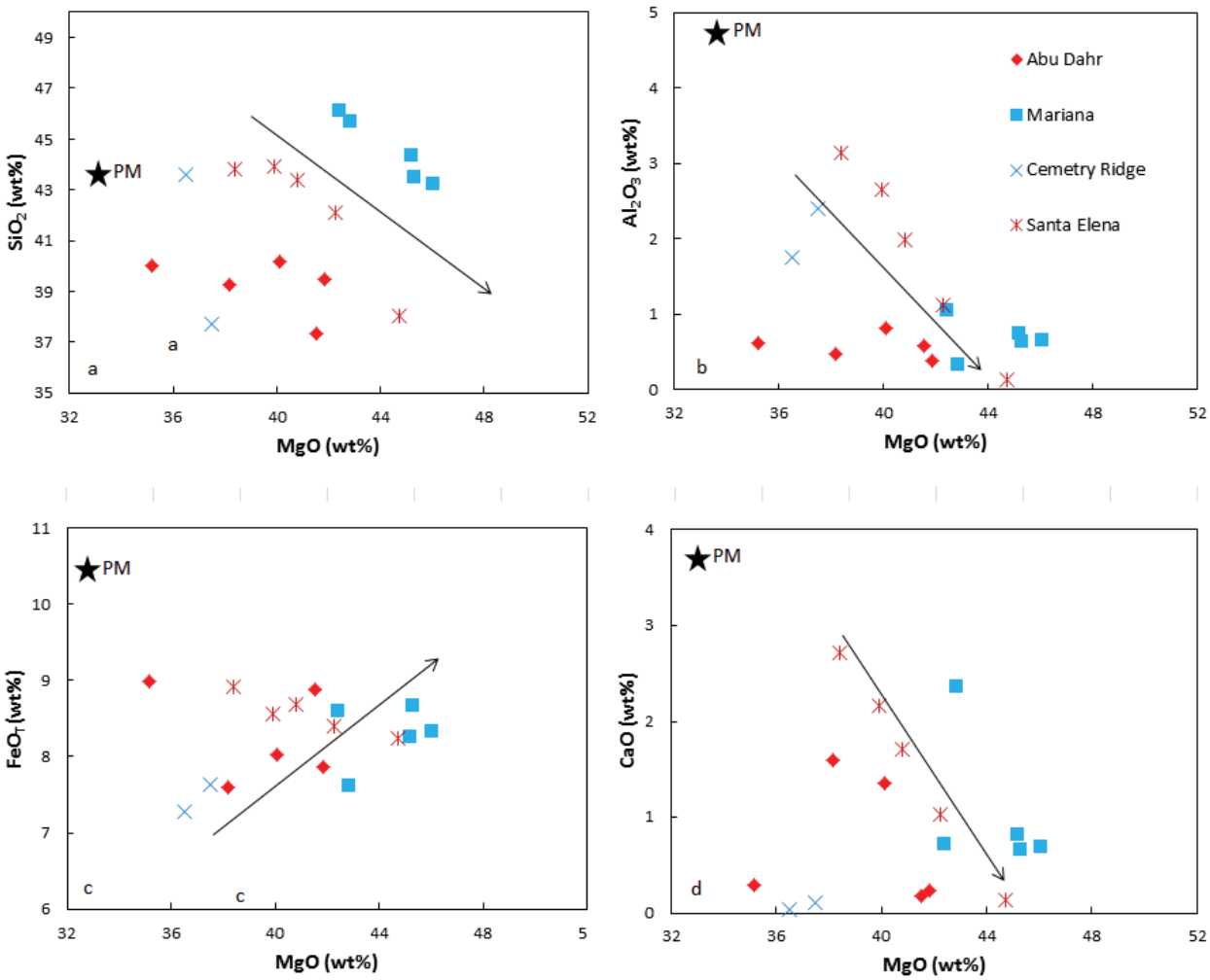

Figure 11

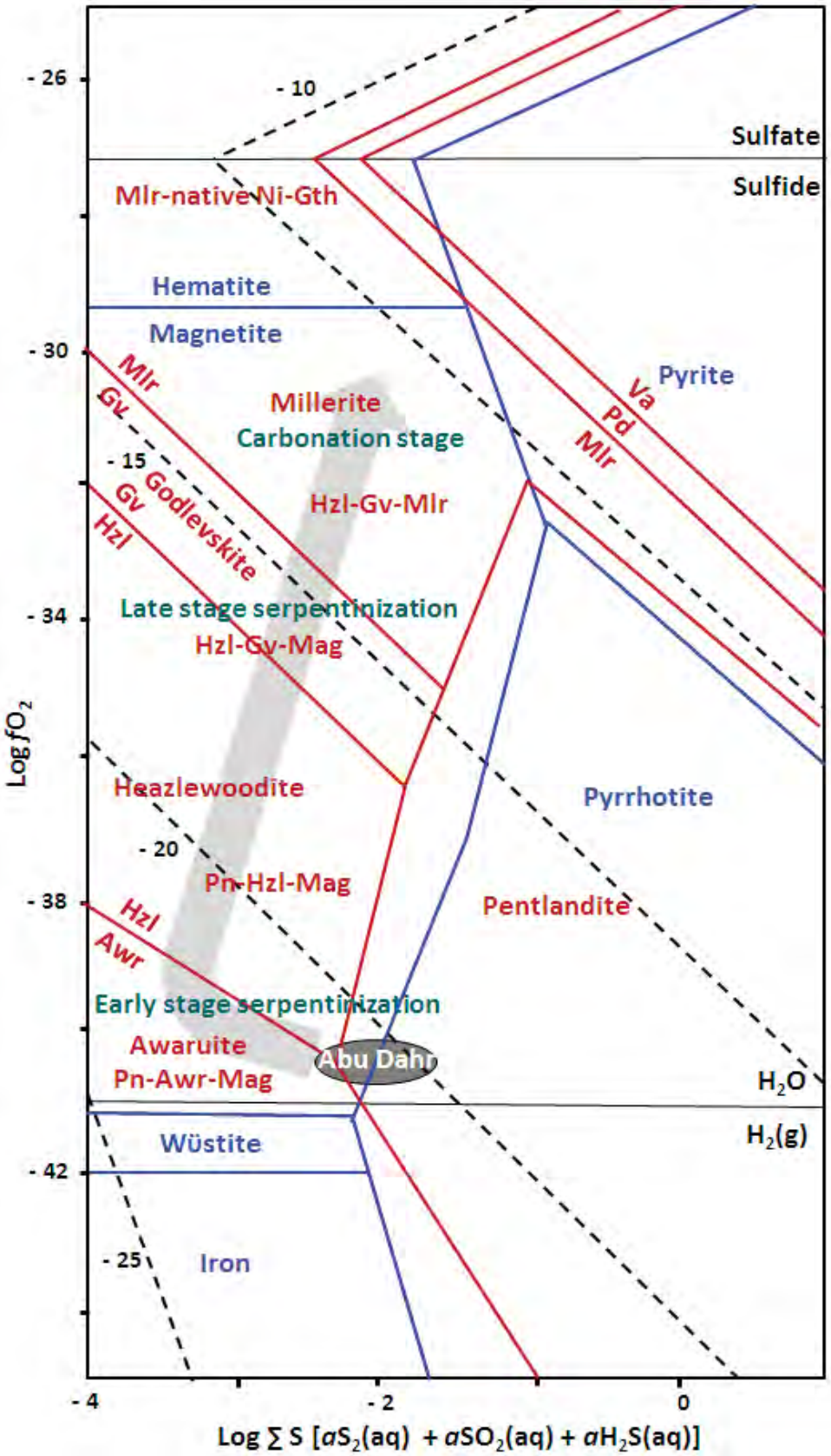

This is the peer-reviewed, final accepted version for American Mineralogist, published by the Mineralogical Society of America.
The published version is subject to change. Cite as Authors (Year) Title. American Mineralogist, in press.
DOI: https://doi.org/10.2138/am-2022-8217. http://www.minsocam.org/

Figure 12